

A NEW APPROACH FOR REDUCING SCATTERED PHOTONS
AND ELECTRON CONTAMINATION IN
COBALT-60 THERAPY BEAM

By

AHMAD AL-BASHEER

A THESIS PRESENTED TO THE GRADUATE SCHOOL
OF THE UNIVERSITY OF FLORIDA IN PARTIAL FULFILLMENT
OF THE REQUIREMENTS FOR THE DEGREE OF
MASTER OF SCIENCE

UNIVERSITY OF FLORIDA

2004

Copyright 2004

by

Ahmad Al-Basheer

بِسْمِ اللَّهِ الرَّحْمَنِ الرَّحِيمِ

قُلْ إِنَّ صَلَاتِي وَنُسُكِي وَمَحْيَايَ وَمَمَاتِي لِلَّهِ رَبِّ الْعَالَمِينَ

صدق الله العظيم

ACKNOWLEDGMENTS

Any project, no matter how individualized, will almost certainly require input, assistance or encouragement from others; my project is no exception.

I extend my sincerest gratitude to Dr. Samim Anghaie. He has been a constant source of thoughtful guidance in pursuing this project. Because of his input, advice and challenge, I have matured as a researcher and as a student. I would also like to acknowledge the contribution of my supervisory committee: Dr. Jatinder Palta, Dr. Jacob Chung and Dr. James Dempsey.

I would also like to take this opportunity to express my sincere gratitude to my classmates and the faculty members in the Nuclear and Radiological Engineering and Radiation Oncology Departments for their constructive suggestions and helpful comments. During my research, I had the pleasure of working at INSPI. With the help of coworkers and friends, even the tedium became bearable. I thank Dr. Travis Knight and Mr. Vadi Samimi for their help. Special thanks go to my family, and mostly Mom and Dad; they have definitely been encouraging me for the longest! They will always be dear to my heart. I would be negligent to not mention the contribution of Carol Mores, in helping me edit my thesis. I thank God for all He has done for me.

TABLE OF CONTENTS

	<u>page</u>
ACKNOWLEDGMENTS	iv
LIST OF FIGURES	vii
ABSTRACT	ix
CHAPTERS	
1 INTRODUCTION	1
Skin Sparing.....	2
Monte Carlo Simulation	3
Incoherent Scattering Spectroscopy	6
2 THEORY OF INCOHERENT SCATTERING.....	9
Scattering.....	9
Coherent Scattering	10
Incoherent Scattering.....	12
3 THEORY AND DISSCUSSION.....	15
Electron Contamination.....	15
Methods of Reducing Electron Contamination	16
Electron Filter	16
Magnetic Field.....	17
Helium Bags	17
Scattered Photons.....	17
The Anti-Scatter Grid	18
Septal Thickness	18
Septal Length.....	20
4 MONTE CARLO SIMULATION.....	22
Scattered Spectrum of Cobalt-60 Beam Simulation	23
The Structure of Calculation.....	25
Primary Spectrum Simulation of Cobalt-60 Machine	25
The Effect of the Lead Filter on Photon Beam Quality.....	33

	The Effect of the Anti-Scattering Grid on Photon Beam Quality	33
5	EXPERIMENTAL SETUP	34
	Choice of Scattering Angle.....	35
	Effects of Collimator	36
	Choice of Shielding Material.....	40
	Choice of Scattering Material.....	41
	Cobalt-60 Therapy Machine	45
	The Collimation System	46
	High Purity Germanium Detector.....	47
	Electronics	48
	Detector Response	50
	Experimental Setup.....	52
6	CONCLUSIONS.....	54
	APPENDIX	
	MCNP INPUT FILE FOR COBALT-60 MACHINE SIMULATION	57
	LIST OF REFERENCES.....	63
	BIOGRAPHICAL SKETCH	66

LIST OF FIGURES

<u>Figure</u>	<u>page</u>
2-1 Atomic form factor versus momentum transfer parameter for carbon and lead (normalized to Z^2).....	11
2-2 Incoherent scattering functions versus momentum transfer parameter for carbon and lead (normalized to Z).....	13
3-1 Minimum path length for all ray passing through the collimator septa from one hole to the next depends on the length and diameter d of the collimator holes and septal thickness.....	19
3-2 Longer septa length allows larger collimator holes since ray passing through two collimator septa with path length or more.....	20
3-3 A cross sectional view of the anti-scatter grid.....	21
4-1 Source capsule design of Theratron 1000 Cobalt-60 therapy machine.....	24
4-2 On-axis energy spectra of photons reaching the scoring plane from Cobalt-60 machine (uncertainty in the peak is less than 0.1%, in the tail is always less than 10 %).	26
4-3 On-axis energy spectra of electrons reaching the scoring plane from Cobalt-60 machine. The spectrum is calculated for scoring region of (uncertainty is less than 10 %).	27
4-4 Photons fluence versus field size reaching a plane at SSD= 80cm. The fluence is scored in a region on the axis.....	28
4-5 On-axis energy spectra of photons reaching the scoring plane from Cobalt-60 machine (uncertainty in the peak is less than 0.1%, in the tail is always less than 10 %).	29
4-6 On axis and off axis scattered to primary photons fluence ratio versus septal thickness at SSD= 80cm. The fluence is scored in a region.	30
4-7 Photons fluence versus field size reaching a plane at SSD= 80cm. The fluence is scored in a region on the axis.....	31

4-8	Electron relative fluence reaching a plane at SSD= 80cm versus lead filter thickness. The number of electrons is normalized to the total photon fluence. The fluence is scored in a region on the axis.....	32
5-1	Optimal scattering angle for different detecting scattered energy ranges and incident photon energy.....	37
5-2	Geometric line broadening for 100 keV photons.....	38
5-3	Geometric line broadening for 1000 keV photons.....	39
5-4	Geometric line broadening for 10 MeV photons.....	39
5-5	The photon cross sections for lead.....	40
5-6	Differential atomic coherent and incoherent cross sections for 100 keV photons in carbon.....	42
5-7	Differential atomic coherent and incoherent cross section for 1250 Kev photons in carbon.....	42
5-8	Differential atomic coherent and incoherent cross sections for 5000 keV photons in carbon.....	43
5-9	Differential atomic coherent and incoherent cross sections for 100 keV photon in lead.....	43
5-10	Differential atomic coherent and incoherent cross sections for 1250 keV photons in lead.....	44
5-11	Differential atomic coherent and incoherent cross sections for 5000 keV photon in lead.....	44
5-12	A schematic electronic system for gamma spectroscopy.....	49
5-13	The experimental setup of coherent and incoherent scattering method (not to scale).....	53

Abstract of Thesis Presented to the Graduate School
of the University of Florida in Partial Fulfillment of the
Requirements for the Degree of Master of Science

A NEW APPROACH FOR REDUCING SCATTERED PHOTONS
AND ELECTRON CONTAMINATION IN
COBALT-60 THERAPY BEAM

By

Ahmad Al-Basheer

May 2004

Chair: Samim Anghaie

Major Department: Nuclear and Radiological Engineering

A new Cobalt-60 beam collimation system is proposed to reduce the contribution of low energy scattered photons. Low energy photons increase the surface dose in radiation therapy procedures involving treatment of sub-surface tumors. The MCNP Monte Carlo code is used to simulate the Cobalt-60 beam from a Theratron 1000 unit, and to calculate the photon spectrum output and electron contamination produced from the photon interaction with the material surrounding the Cobalt source. Using 1 mm thick lead filter can minimize the presence of electron contamination. An anti-scattering grid is proposed to reduce the scattered photons fluence reaching the treatment surface. The use of such a grid helped in reducing the contribution of scattered photons by 40%.

While the knowledge about the spectral information from high-energy x-ray machines is fundamental in such an application, how to get the information presents a daunting task. The difficulty lies in the fact that the detector is in an intense field of

billions of particles bombarding it, and will be saturated instantly. In addition, the detecting efficiency falls off drastically at high energy. To remedy this saturation, an experiment based on the scattering method is designed. The scattering method can effectively reduce the high intensity, and the energy spectrum is shifted to lower energy range. However, in applying this method to a practical situation, attention should be paid in setting up the components of the experiment.

In this research project, a complete formulation for the incoherent scattering method is given; the theory behind the anti-scattering grid is presented. When both the electron filter and the anti-scattering grid are applied, scattered photon and electron contamination fluence are reduced by 40 and 90%, respectively.

CHAPTER 1 INTRODUCTION

For almost half a century, cobalt has been shown to effectively treat cancer, thereby improving quality of life. The continued strong demand for cobalt therapy attests to its universal acceptance as a modality in the treatment of cancer worldwide. In many countries, cobalt therapy is viewed as an indispensable tool for modern treatment facilities known for its effectiveness, productivity and dependability. In addition to the low cost of maintaining Cobalt-60 machines comparing to other therapy equipment, Cobalt-60 offers an entirely predictable output that is totally unaffected by temperature, humidity, power supply or other external influences.

Despite all of the advantages of Cobalt-60, most radiotherapy treatment plans are carried using linear accelerators. Many reasons contribute to this fact; large penumbra for Cobalt-60 due to geometrical factor, multiple energies that can be provided by the accelerator, the capability of electron beam production, skin sparing or simply the fact that many institutes compete to carry the latest technology available.

However, the current generation of three-dimensional treatment planning systems, networked to commercial block and compensator cutters, could provide the means for high quality radical radiotherapy treatments on cobalt units. In addition, the recent availability of intensity modulation planning modules for such systems may provide further potential for state-of-the-art radiotherapy treatments on this hitherto mature treatment modality.

Jim Warrington and Liz Adams (2002) had measured the penumbra of a Theratron 780 head containing 1.75 cm diameter source. The width of the 20-80% cobalt unit penumbra was within the range of linac x-ray beams, even leaving aside the effective penumbral broadening of multi-leaf collimator (MLC). They also showed that by using the TMS treatment planning system with its IMRT and non-coplanar, conformal planning software, they have been able to demonstrate that comparable quality external beam treatment planes can be achieved using a cobalt unit, when compared to a linear accelerator. They include lesions in the brain, thyroid and a deep-seated prostate volume in the pelvis.

Skin Sparing

One of the most important challenges that face radiotherapy in general is the dose delivered to the patient skin. When a patient is treated with a mega-voltage beam, the surface dose or skin dose can be substantially lower than the maximum dose that occurs in the subcutaneous tissue. In contrast to lower energy beams, which give rise to maximum ionization at or close to the skin surface, the mega-voltage beams produce an initial electronic buildup with depth, resulting in a reduced dose at the surface and maximum dose at the equilibrium depth.

However, a significant dose is delivered to patient skin in any therapeutic session using Cobalt-60 machine. Surface dose results from scattered radiation as well as electron contamination of the incident beam. The effect of electrons generated in the air was studied by placing a He gas-filled plastic bag in the beam. A value of about 12% is estimated for the lowest relative dose attainable with a polystyrene phantom in a “clear” Cobalt-60 gamma ray beam of 1 cm diameter (Attix et al.1982). An alternative way for electron filtration is the magnetic field (Biggs and Ling 1979, Ling and Schell 1982).

These investigations proved that electrons were a principal beam contaminant. However, the routine removal of electron contamination by magnetic means is not regarded as a practical procedure due to weight, space and cost considerations.

Several studies have shown that using an electron filter is an effective and simple way to reduce electron contamination (Biggs and Ling 1979, Biggs et al. 1987, Galbraith and Rawlinson 1985). Ling and Biggs reported that a 0.55-g/cm^2 -thick lead foil was an optimal electron filter for a 25-MV linac. They also pointed out that lead was the overall best material for the purpose of filtering secondary electrons. From a study of three 10-MV accelerators, Rao et al. 1988 showed that Pb could be used as an effective filter material for field sizes up to $30 \times 30\text{ cm}^2$.

New approaches for filtering out contaminate electrons and scattered photons are proposed in this work. The principle of anti-scattering grid is reviewed based on the used material and design. The purpose of the grid is to filter out scattered photons. A thin sheet of lead was added beneath the grid to remove contamination electrons. To study this new approach, Monte Carlo simulation techniques were used.

Monte Carlo Simulation

The Monte Carlo simulation technique has found widespread application in the radiological sciences (Morin 1988). The use of Monte Carlo application in medical physics has been reviewed by Mackie (1990) and Andreo (1991). This expanded utilization is due to the available computing power and the accessibility of software packages (e.g., EGS4/BEAM, GEANT, MCNP).

Several researchers have carried out direct Monte Carlo simulations of the treatment head design in order to provide spectral data. For a series of beam energies

Mohan et al. (1986) calculated spectra that later were frequently used as a standard set. They also studied the lateral variation in beam spectrum and characterized it in terms of half-value thickness. Lovelock et al. (1995), Liu et al. (1997) and DeMarco et al. (1998) applied Monte Carlo techniques to generate beam spectra and all found that the incident electron beam energy must be tuned in order to obtain agreement with measured depth dose data.

EGS Monte Carlo code was used by Han et al. (1987) to compute photon spectra from an AECL Theratron 780 Cobalt-60 unit. They concluded that the observed increase in output of the machine with increasing field size is caused by scattered photons from the primary definer and the adjustable collimator of the unit. They also showed the photon spectrum reaching the surface of a patient for a fixed source-to-surface distance (SSD). It is known that the energy spectrum consists not only of the 1.17 and 1.33 MeV primary photon lines, but also of a broad distribution of photons of lower energies resulting mainly from Compton interactions. These spectra were then used as input to a pencil-beam model to calculate tissue-air ratios in water. This result was compared with a calculation that assumes a monochromatic photon energy of 1.25 MeV and measured data. The agreement among the three curves was good up to a depth of 10 cm. Beyond that point, the dose contribution calculated for 1.25 MeV photons was higher than the dose calculated using a more realistic spectrum. Recently, Mora et al. (1999) used the BEAM (Rogers et al. 1995) Monte Carlo code to simulate the Cobalt-60 beam from an Eldorado 6 radiotherapy unit and to calculate the relative air-keram output factors as a function of field size; this unit is more realistically modeled. The calculated relative air-kerma output factor at SSD=80.5 cm agrees to within 0.1% with measured values. It is

shown that the variation of the output factor is almost entirely due to scattered photons from the fixed and adjustable collimator and there is no effect of shadowing primary photons. The influence of the geometry of the collimating system on the photon spectra on-axis is shown to be small but finite. The calculated buildup region of a depth-dose curve in a water phantom irradiated by a narrow and broad Cobalt-60 beam is shown to agree with experimental data at 2% and 3% levels. Unlike prior calculations, their results accurately predict the effect of electron contamination from the surface to dose maximum. The field size is shown to have some effect on the photon spectra.

The MCNP (Briesmeister 1997) Monte Carlo code has been employed by Lewis et al.(1999) to calculate the energy spectra and angular distribution of x-ray beams for the Philips SL75/5 linear accelerator in a plane immediately beneath the flattening filter. These data were subsequently used as a “source” of x-rays at the target position, to assess the emergent beam from the secondary collimators. The depth dose distribution and dose profile at constant depth for various field sizes have been calculated for nominal operating potential of 4 MV, and found to be within acceptable limits. Analysis of the x-ray spectra shows that the energy-weighted mean energy (i.e., the relative number of x-rays in each interval multiplied by their energy) leaving the target, the primary collimator, flattening filter and secondary collimators is 1.16, 1.32, 1.31, and 1.28 MeV, respectively, assuming a second collimating setting of $10 \times 10 \text{ cm}^2$. The overall mean x-ray energy of the emergent beam from the secondary collimators, 1.28 MeV, agrees with the generally perceived value of one-third the maximum energy. In the central part of the beam, as expected, the flattening filter has the largest influence on hardening. The variation in fluence-weighted x-ray energy with radial distance of the filtered and

unfiltered 4 MV beams was also compared. The result showed that the filtered and unfiltered beams had approximately the same fluence-weighted x-ray energy at a distance of 4 cm away from the central axis within the linear accelerator head and also the preferential filtration of the lower energy components by the filter.

The principal advantage of the Monte Carlo method is that it can be used to obtain angular distributions and quantities that can hardly be measured experimentally. The second advantage is that the energy spectrum can be generated in regions away from the central axis simultaneously. The third advantage is the possible savings in manpower at the expense of the large amount of CPU time of computers. In theory, this method provides an accurate means of obtaining the energy spectrum and angular distribution. In addition, the Monte Carlo method can be used to simulate the energy distribution and angular distribution of electrons, thus providing insights on electron contamination on photon beams or photon contamination on electron beams (Petti et al. 1983a, Petti et al. 1983b). The accuracy of the Monte Carlo method is limited to the modeling of the machine head construction and assumptions made concerning the electron beam incident on the target, pre-assuming that the particle transport models, including cross section data, are accurate. The drawback of such simulation is the lack of tractability to measured quantities.

Incoherent Scattering Spectroscopy

An experiment was designed to check the output of the MCNP simulation. This experiment was based on the incoherent scattering spectroscopy (ISS). This method has been tried on several occasions in the past to deduce the energy spectra (Bentley et al. 1967, Levy et al. 1974, 1976, Faddegon et al. 1990, 1991, Landry and Anderson 1991). In this method, a small scattering material is put in the beam, and the once-scattered

spectrum is then measured at a certain angle, so that from the scattered spectrum it is relatively simple to deduce the original spectrum. The scattered radiation intensity incident on the detector is reduced by several magnitudes by the scattering process; furthermore, the energy of the scattered photons is reduced as well because of the incoherent scattering, so that a more suitable energy range for the detector is obtained. The angular distribution of photons can be measured by scanning the small scatter in the radiation field. Most of the measurements were done with NaI (Tl) detectors, but the poor resolution inherent to this type of spectrometer renders the information less valuable. With the advent of the HPGe detector, its superb energy resolution provides an ideal technique for accurate measurement of spectral information for x-rays.

A drawback of the incoherent scattering method is that higher energy photons have a smaller probability of being scattered than do lower energy photons. Also, they suffer a greater fractional decrease in their energy on incoherent scattering; this method results in a reduction of resolution. To demonstrate this effect quantitatively, a mono-energetic source and a spectrometer with good spectral resolution are needed. Also, in the incoherent scattering method, it is necessary to define an accurate scattering angle. This procedure needs a collimator, which not only causes distortion in measured spectrum, but also increases the difficulty in alignment.

The present work is a study of Cobalt-60 beam quality specification with emphasis on the reduction of the scattered photons and contamination electrons. This reduction will increase skin sparing. The calculation conducted in this study shows that using a high Z anti-scattering grid can substantially reduce the fluence of scattered photons without increasing the electron contamination. In order to fully understand reliability, application

and the limitation of the new approach proposed, a series of Monte Carlo simulation are performed with the Cobalt-60 therapy machine.

CHAPTER 2 THEORY OF INCOHERENT SCATTERING

Scattering

The theory of the scattering method is based on two major scattering types: coherent and incoherent scattering. If $I(E_o)$ photons/sec of energy E_o are incident on the scattering material with atomic number Z and thickness Δx , then the number $D(E)$ of photons/sec scattered at a certain angle θ and incident on a detector which subtends solid angle $d\Omega$ (ignoring the attenuation in the scatter itself if the scatterer is small) is given by:

$$D(E)dE = [N\Delta x\Delta\Omega\varepsilon(E)]\left(\frac{d\sigma_{Coh}}{d\Omega} + \frac{d\sigma_{Incoh}}{d\Omega}\right)I(E_o)dE_o, \quad (2-1)$$

where E_o and E are the energies of the incident and once-scattered photons, Z is the atomic number of the scattering material, Δx is the thickness of the scatterer, N is the number of atoms in the relevant scattering volume, $\varepsilon(E)$ is the efficiency of the detector, and $\Delta\Omega$ is the solid angle subtended by the pinhole of the collimator in front of the detector. The atomic differential coherent scattering cross section and incoherent scattering cross section are given below:

$$\frac{d\sigma_{Coh}}{d\Omega} = \frac{r_0^2 (1 + \cos^2 \theta)}{2} F^2(x, Z) \quad (2-2)$$

$$\frac{d\sigma_{Incoh}}{d\Omega} = \frac{d\sigma_{KN}}{d\Omega} S(x, Z) = \frac{r_0^2}{2} \left(\frac{E}{E_0} \right)^2 \left(\frac{E}{E_0} + \frac{E_0}{E} - \sin^2 \theta \right) S(x, Z), \quad (2-3)$$

where $r_0=2.818 \times 10^{-13}$ cm is the classical radius of the electron, $x=\sin(\theta/2)/\lambda$ is the momentum transfer parameter, λ is the wavelength of the incident photons, θ is the scattering angle of the photon (defined as the angle between the direction of flight before and after the interaction), $d\Omega=2\pi\sin\theta d\theta$ is the solid-angle element, $F(x, Z)$ is the atomic form factor and $S(x, Z)$ is the incoherent scattering function.

Coherent Scattering

For low-energy photons or small-angle scattering, the energy transferred to the struck electron is small compared with the binding energy of the electron. The atom is neither ionized nor excited, and the entire atom absorbs the recoil momentum. Under these conditions, the energy of the photon scattered by the bound electrons of an atom is essentially the same as that of the incident photon, and no energy is deposited. There is a fixed-phase relationship among the scattered x-rays, which are thus capable of producing constructive interference. This process is called coherent scattering or Rayleigh scattering. It is most prominent for low-energy photons scattered in high Z material. Eq. (2-2) gives the atomic differential cross section per atom for unpolarized radiation.

$F(x, Z)$ is the atomic form factor that can be theoretically calculated by partially-relativistic or relativistic quantum mechanics. While Hubbel et al. (1975) compiled the partially-relativistic quantum mechanics calculation results, more accurate and complete compilation was done by Chantler (1995). Figure 2-1 shows the atomic form factors of carbon ($Z=6$) and lead ($Z=82$). As can be observed, $F(x, Z)$ is approximately equal to Z

for momentum transfers smaller than that typical of orbital electrons. As the momentum transferred exceeds this typical value, the electrons are less likely to scatter photons

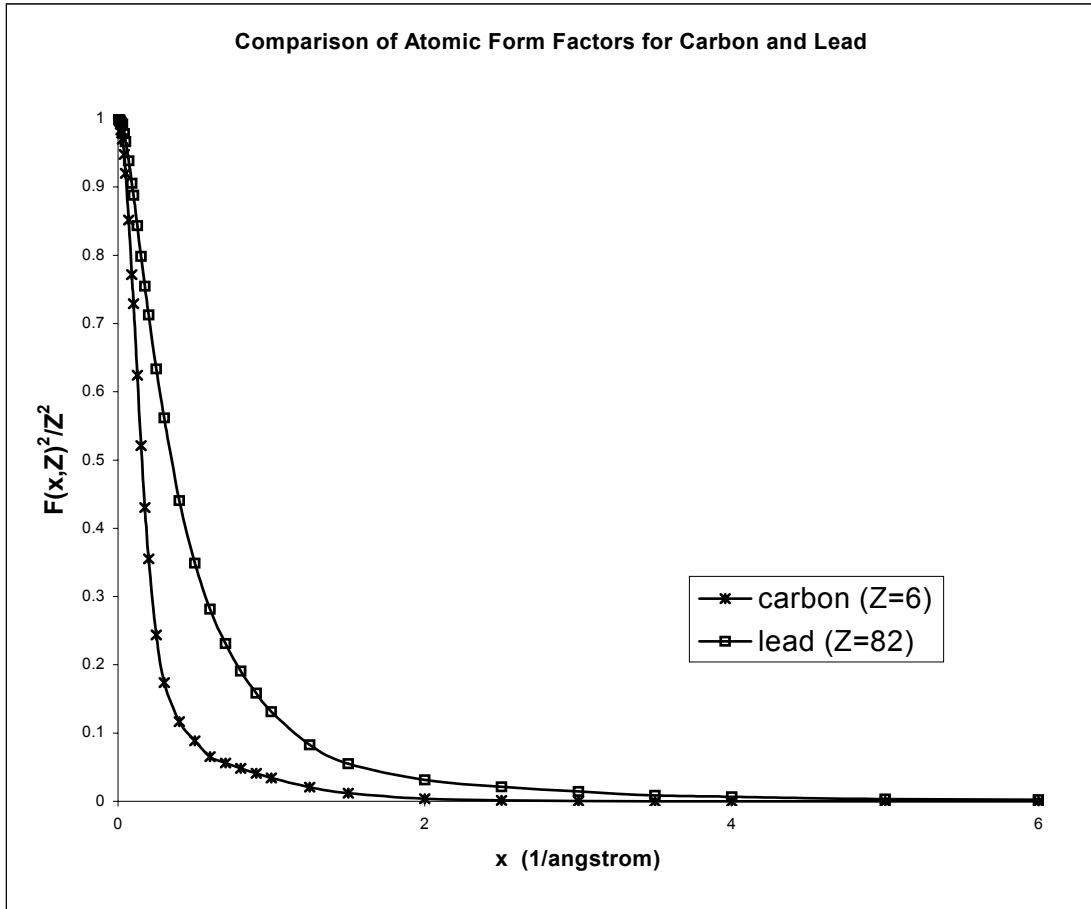


Figure 2-1. Atomic form factor versus momentum transfer parameter for carbon and lead (normalized to Z^2).

elastically, causing the form factor to fall off rapidly with increasing scattering angle and incident photon energy. The result is a highly anisotropic, forward-peaked angular scattering distribution. The square of the atomic form factor $F(x, Z)$ represents the probability that the Z electrons take up the recoil momentum, without absorbing any energy from the photon.

Incoherent Scattering

Incoherent scattering, often identified with the Compton effect, is an inelastic collision between an atom and an x-ray photon in which the orbital electrons retain part of the photon energy, altering both the energy and flight path of the incident photon. For small-scattering angles and low-energy incident x-rays, the recoil energy of the electron would be comparable to, or smaller than, the electron binding energy, especially for heavy elements. Thus, the assumption that the electron is initially free and stationary may not apply. The deviation from the free electron cross section is greatest for the inner-shell electrons, and becomes negligibly small for the loosely bound valence electrons.

Therefore, the correction to the Klein-Nishina collision cross section depends upon the atomic number Z and should be expressed on a per atom basis. To a close approximation, the probability can be expressed as the product of the Klein-Nishina cross section and the incoherent scattering function, $S(x, Z)$, which is shown by Eq. (2-3). The latter factor represents the probability that an atom will be raised to an excited or ionized state when a photon imparts a recoil momentum to an atomic electron. The momentum transfer parameter is given by:

$$x = \frac{m_0 c}{2h} [E_0^2 + E^2 - 2E_0 E \cos \theta]^{1/2}, \quad (2-4)$$

where m_0 , c , and h denote electron rest mass, velocity of light, and Planck's constant, respectively. Since the binding corrections are only important for small momentum transfers, an approximation is often made for the purpose of computing x . This allows use of the simple expression, $x = \sin(\theta/2)/\lambda$, for both coherent and incoherent scattering. The error introduced into the differential cross section by this

approximation does not exceed 1-2%. The incoherent scattering function can therefore be expressed in terms of the same variable, x , defined previously for the form factors. The incoherent scattering functions have been tabulated along with atomic form factors for all elements. The factor $S(x, Z)$ increases rapidly, especially for low Z elements, at small values of x , and approaches a maximum value of Z at large values of x . Therefore, the incoherent scattering function modifies the Klein-Nishina cross section most prominently for small-angle scattering of low-energy photons in high Z elements under conditions where the effect of electron binding is strong. Figure 2-2 shows the incoherent scattering functions for carbon and lead plotted as a function of x . This graph illustrates the dependence of the effect of electron binding on the atomic number.

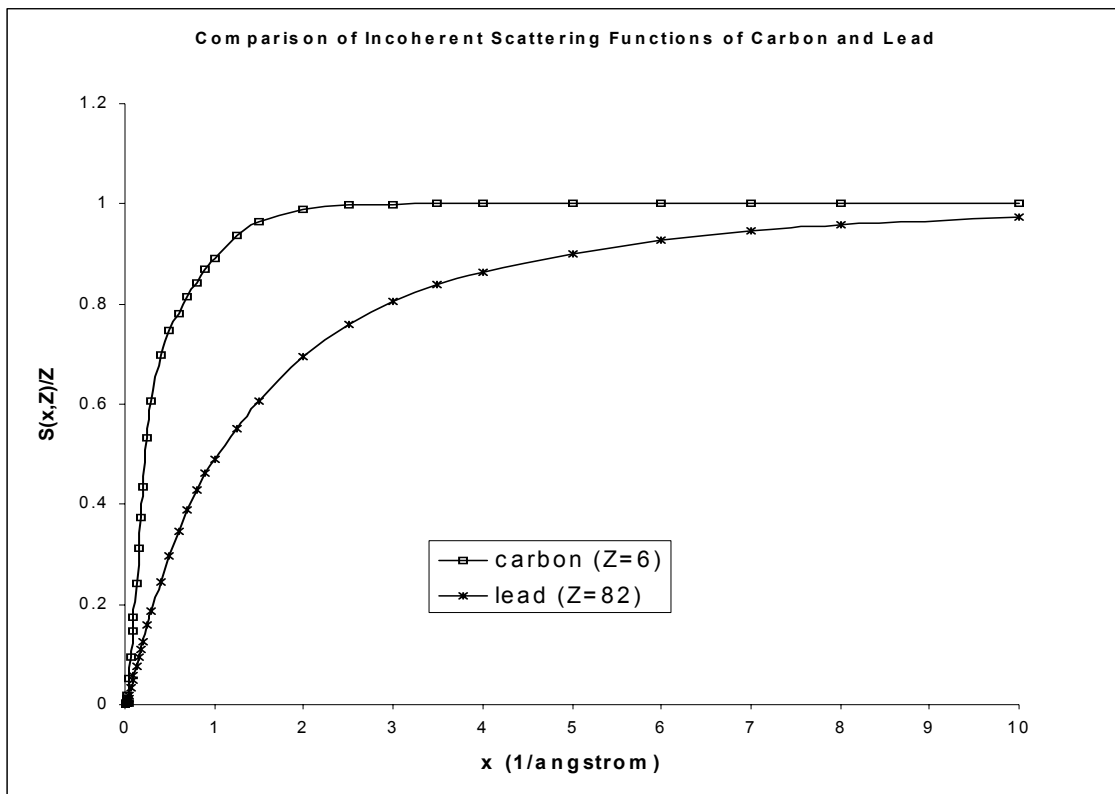


Figure 2-2. Incoherent scattering functions versus momentum transfer parameter for carbon and lead (normalized to Z).

The electron binding effect also introduces a small deviation in the Compton energy shift of the photon. Since the effective mass of a bound electron tends to be slightly increased, the energy transferred to a bound electron is less than that transferred to a free electron. Nevertheless, this change in energy shift is negligibly small, so that modification of the angular distribution of the scattered photon alone will be adequate in a photon diffusion model.

The original spectrum incident on the scatterer can then be deduced by rearranging terms from Eq. (2-1):

$$I(E_o) = \left(\frac{D(E)}{[N\Delta x \Delta \Omega \varepsilon(E)] \frac{d\sigma_{Coh}}{d\Omega}} \right) \frac{dE}{dE_o} + \left(\frac{D(E)}{[N\Delta x \Delta \Omega \varepsilon(E)] \frac{d\sigma_{Incoh}}{d\Omega}} \right) \frac{dE}{dE_o}. \quad (2-5)$$

In the case of insignificant coherent scattering, Eq. (2-5) is reduced to:

$$I(E_o) = \left(\frac{D(E)}{[N\Delta x \Delta \Omega \varepsilon(E)] \frac{d\sigma_{Incoh}}{d\Omega}} \right) \frac{dE}{dE_o} = \left(\frac{D(E)}{[N\Delta x \Delta \Omega \varepsilon(E)] \frac{d\sigma_{Incoh}}{d\Omega}} \right) \left(\frac{E}{E_o} \right)^2. \quad (2-6)$$

CHAPTER 3 THEORY AND DISCUSSION

When a patient is treated with a mega-voltage beam, the surface or skin dose can be substantially lower than the maximum dose that occurs in the subcutaneous tissues. In contrast to lower-energy beams, which gives rise to maximum ionization at or close to skin surface, the mega-voltage beams produce an initial electronic buildup with depth, resulting in a reduced dose at the surface and maximum dose at the equilibrium depth.

Skin sparing is one of the most desirable features of high-energy photon beam. However, this effect may be reduced or even lost if the beam is excessively contaminated with secondary electrons or back-scattered radiation (both electrons and photons).

Electron Contamination

Electron contamination of the incident beam and back-scattered radiation, including electrons and photons from the medium, are the reasons behind surface dose. Photon interactions in the collimator, air and any other scattering material in the path of the beam, produces secondary electrons that contaminates all x-ray and gamma-ray beams used in radiotherapy. For example, an increase in skin dose can be made during a photon therapy session if a shadow tray is used to support beam-shaping blocks and secondary electrons are produced by photon interaction in the tray. However, a shadow tray is usually thick enough to absorb most of the electrons incident on the tray.

Methods of Reducing Electron Contamination

Improvements in the beam purity and skin sparing can be achieved through (i) reduction in beam size to allow electrons to scatter out (Harper et al 1991, Klevenhagen et al 1991), (ii) magnetic removal of electrons (Biggs and Ling 1979, Ling et al 1982), (iii) use of medium-to-high Z filters that scatter contaminant electrons out of the beam without generating appreciable additional electrons (Leung and Johns 1977, Ling and Biggs 1979, Ciesielski et al. 1989, Nilsson 1985 and Roa et al. 1988), and /or (iv) replacing the air that the beam passes through by helium in a thin plastic bag (Attix et al 1983 and Yorke et al. 1985).

Electron Filter

Several studies have shown that using an electron filter is an effective and simple way to reduce electron contamination (Ling and Biggs 1979, Biggs et al. 1987, Galbraith and Rawlinson 1985 and Parthasaradhi et al. 1989). Ling and Biggs reported that a 0.55 g/cm^2 thick lead foil was an optimal electron filter for a 25 MV linac. They also pointed out that lead was the overall best material for the purpose of filtering secondary electrons. From a study of three 10 MV accelerators, Rao et al. showed that Pb could be used as an effective filter material for field sizes up to $30 \times 30 \text{ cm}^2$. Rogers et al. did a Monte Carlo calculation of electron contamination in a Cobalt-60 therapy beam. They reported that a 0.075 cm thick copper filter, placed immediately behind the head, creates a considerable reduction in electron contamination. For a 6 MV linac, Parthasaradhi et al. observed that the electron contamination of both the open beam and the beam with the tray can be effectively reduced by placing a lead filter immediately below the blocking tray, which was located at a distance of 61.5 cm from the source. They noticed that the

differences in percentage depth dose between the open and the filtered beam were less than 2%.

Magnetic Field

An alternative to solid transmission-type filters for removing electrons from photon beams is the magnetic field (Ling et al 1982 and Biggs and Ling 1979). These investigations proved that electrons were a principal beam contaminant. However, the routine removal of electron contamination by magnetic means is not regarded as a practical procedure due to weight, space and cost considerations.

Helium Bags

The replacement of plastic bags filled with helium is a well-known method employed in high-energy accelerators for reducing the scattering of particle beams after they leave a vacuum system. It offers a way to reduce, by a factor of seven, the mass of material and the number of electrons per unit volume in the space through which the photon beam passes. A vacuum tank is not as efficient, because electrons generated in the exit window recontaminate the beam. The corresponding recontamination by a thin plastic bag is very slight (Attix et al. 1983).

Scattered Photons

There has been a controversy as to the relative contribution of secondary electrons versus low-energy scattered photons to dose in the buildup region. The bottom line is that both factors contribute significantly in dose delivered to the buildup region of the patient.

Most of the scattered photons contributing to the skin dose from Cobalt-60 are produced by three components; source capsule, primary and adjustable collimator and the lead shield. The source region, which includes primary and adjustable collimator, has the highest impact on the percentage of photons scattered. The number of primaries and the

number of photons scattered only by the source region remain relatively constant as the field size increases. The photons from the source region include a component from the lead shield surrounding the primary collimator and source capsule.

The primary and adjustable collimator effect varies depending on the field size. As the field size increases, a higher percentage of scattered photons will be allowed to reach the patient. However, the effect of both collimators is less than 10% on the scattered beam spectrum.

It is well known that as the field size increases, the depth dose in the buildup region increases, resulting in a shift in the depth of maximum dose, d_{\max} , to increasingly shallower depths. Current evidence favors the hypothesis that the effect is predominantly caused by the secondary electrons.

Only 28 particles reach the front face of the capsule for every 100 photons from Cobalt-60 decay. At the front face of the capsule most particles are photons, and electrons represent only .05% of the particles. These electrons have an average energy of 616 keV. Scattered photons represent 28% of the photon fluence at the front face of the capsule.

The Anti-Scatter Grid

The principle of absorption collimator for scattered radiation is employed. An absorptive collimator allows only those gamma rays traveling in their original direction to penetrate and scattered radiation with lower energies and different direction from their initial one to be absorbed. Figure 3-1 explains the idea of this collimator.

Septal Thickness

A primary consideration in the design is to ensure that septal penetration by gamma rays crossing from one collimator hole into another is small. This is to reduce the

scattered radiation from the geometry behind the collimator. No thickness of septal material is sufficient to stop all gamma rays, so the usual criteria is to accept some reasonable small level of septal penetration.

The required septal thickness may be determined by analysis of Figure 3-1. The shortest path length for gamma rays to travel from one hole to the next is w . Septal thickness t is related to w , the length l and diameter d of the collimator holes, by

$$t = 2dw/(l - w) \quad (3-1)$$

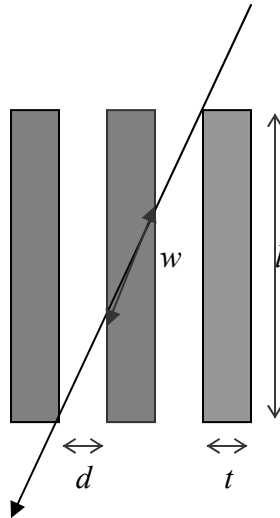


Figure 3-1. Minimum path length w for all γ ray passing through the collimator septa from one hole to the next depends on the length l and diameter d of the collimator holes and septal thickness t .

If septal penetration is to be less than certain percentage p , the transmission factor for the thickness w must be

$$e^{-\mu w} \leq p \quad (3-2)$$

where μ is the linear attenuation coefficient of the septal material.

$$t \geq \frac{2d(\ln(\rho) / \mu)}{l - (\ln(\rho) / \mu)} \quad (3-3)$$

Therefore, it is desirable that septal thickness t be as small as possible, so that the collimator septa obstruct the smallest possible area to allow higher output from the Cobalt-60 machine. This objective is realized by using a material with a large value of μ for collimator septa. Material of high atomic number Z and high density ρ are preferred. Lead ($Z=82$, $\rho=11.34 \text{ g/cm}^3$) is the material of choice for reasons of cost and availability; however, other material including tantalum ($Z=73$ $\rho=16.6$) and tungsten ($Z=74$ $\rho=19.4$) will achieve the same goal.

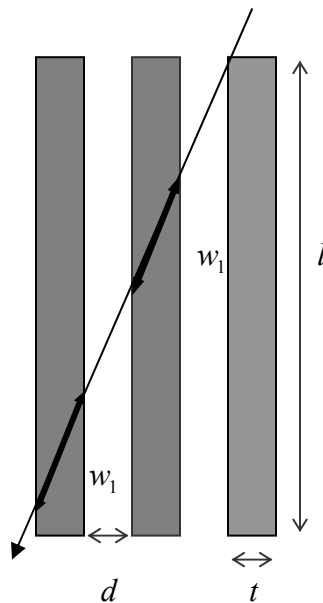


Figure 3-2. Longer septa length l allows larger collimator holes since γ ray passing through two collimator septa with path length $w_1 + w_2$ or more.

Septal Length

The anti-scattering grid can occupy smaller areas by using longer septa “thicker collimator”. As shown in Figure 3-2, the probability that scattered radiation can be

absorbed by more than one septa is higher if longer septa are used. Thinner septa will result in the same amount of attenuation and eventually less area to be occupied.

These septa have to be arranged next to each other as adjacent cones to fit the fan-shape beam produced by the Cobalt-60 source. As shown in Figure 3-3, all of these cones have to have their vertices located at the center of the source used, allowing primary beam to penetrate and scattered beam to be absorbed.

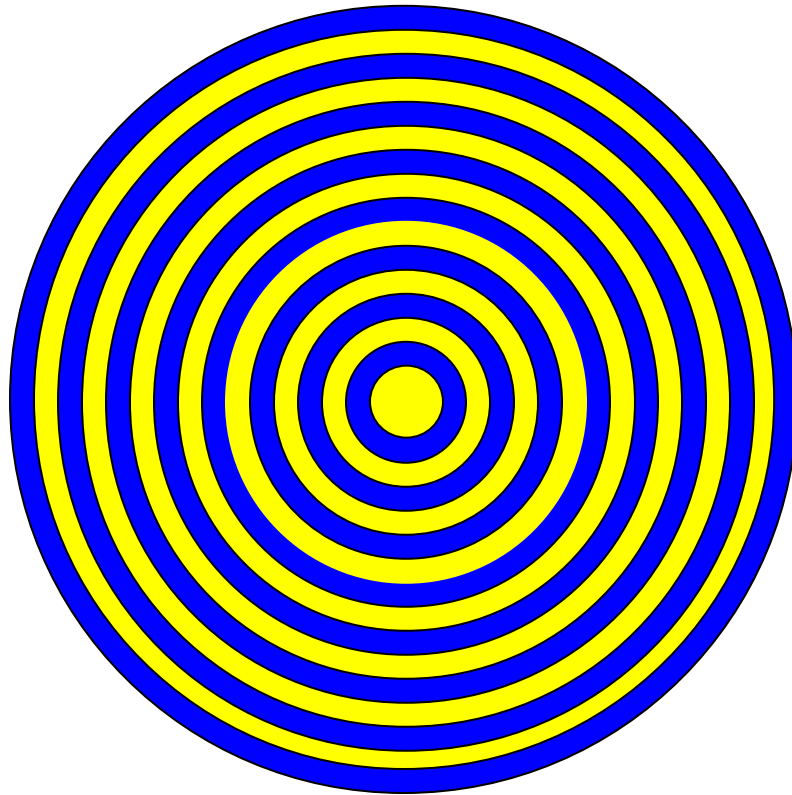


Figure 3-3. A cross sectional view of the anti-scatter grid.

CHAPTER 4 MONTE CARLO SIMULATION

The Monte Carlo simulation technique has found widespread application in the radiological sciences (Mackie 1990 and Andreo 1991). Monte Carlo simulation of photon beam transport has proven to be a valuable tool to determine and optimize the accuracy and effectiveness of experimental measurements; it can also provide information which is otherwise inaccessible.

The simulations were performed by means of the Monte Carlo code MCNP (Monte Carlo N-Particles, version 4B) (Briesmeister 1997). The code allows transport of photons (in the energy range from 1 keV up to 100 MeV), neutrons (between 10^{-11} and 20 MeV) and electrons (between 1 keV and 100 MeV) through matter. For photons, MCNP has two interaction models: simple and detailed. The simple physics treatment ignores coherent (Thomson) scattering and fluorescent photons from photoelectric absorption. It is intended for high-energy photon problems, or problems where electrons are free, and is also important for next event estimators such as point detectors, where scattering can be nearly straight ahead with coherent scatter. The detailed physics treatment includes coherent scattering and accounts for fluorescent photon after photoelectric absorption. Atomic form factors are used to account for electron binding effects. The detailed physics treatment is almost always used by default. It is the best treatment for most applications, particularly for high Z nuclides or deep penetration problems.

The generation of electrons from photons is handled in one of three ways. These three ways are the same for both the simple and the detailed photon physics treatments:

- (1) If electron transport is turned on (Mode P E), then all photon collisions except coherent scatter that can create electrons are banked for later transport.
- (2) If electron transport is turned off (no E on the Mode card), then a thick-target bremsstrahlung (TTB) model is used; this model generates electrons, but assumes that they travel in the direction of the incident photon and they are immediately annihilated. Any bremsstrahlung photons produced by the non-transported electrons are then banked for later transport. Thus, electron-induced photons are not neglected, but the expensive electron transport step is omitted.
- (3) If IDES=1 on the PHYS: P card, then all electron production is turned off, no electron-induced photons are created and all electron energy is assumed to be locally deposited. The TTB approximation cannot be used in Mode P E problems, but it is the default for Mode P problems.

To use MCNP code, the user must create an input file containing pertinent information to define the geometry, source and material. The code also offers a variety of tallies with which the concerned interaction can be scored. The variance reduction techniques offered by MCNP reduce the error and calculation time.

Scattered Spectrum of Cobalt-60 Beam Simulation

The first simulation is a simplified design of Cobalt-60 machine, where a fan-shaped beam is generated from a Cobalt-60 source with photons energy 1.172 and 1.33 MeV. The Cobalt-60 source is simulated as a cylinder with a radius of 0.75 cm and height of 3.05 cm. Ge detector is a cylinder of 2 cm radius. The source-surface of the detector distance SSD is 80 cm. The spectrum result is shown in Figure 4-2.

As shown in Figure 4-2, the spectrum of the Cobalt-60 machine is a continuous spectrum, consisting of predominantly 1.172 MeV and 1.33 MeV photons with degraded photons from beam defining systems.

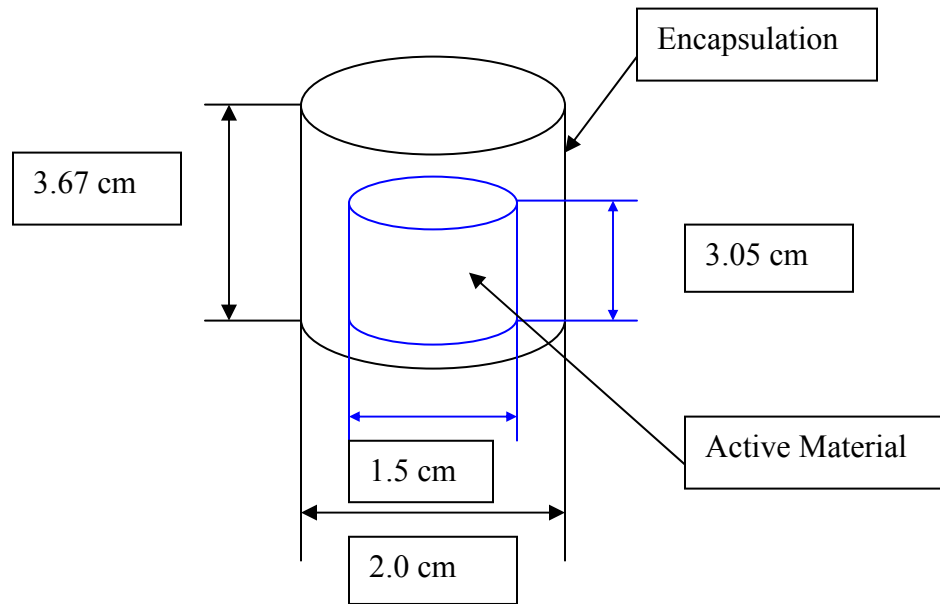


Figure 4-1 Source capsule design of Theratron 1000 Cobalt-60 therapy machine.

The Theratron 1000 model is a typical Cobalt-60 therapy unit. It consists of a source capsule which contains radioactive Cobalt-60 pellets, an immovable primary collimator, an outer set of movable collimators which define the various field sizes of the therapy beam and an overall shielding for radiation protection. Particular attention has been paid to the careful modeling of the geometry and construction of three of its main components: the Cobalt-60 source capsule, the source housing and the collimator assembly. Although simplified in the modeling process, the most important features of each of these components have been retained. Figure 4-1 shows a drawing of the source capsule.

Previous simulation shows that the nickel-plating of the pellets has little effect on the spectrum, so the active material is modeled as homogenous Cobalt-60. In our MCNP simulation, we have used a value 1.5 for the diameter of the Cobalt-60 capsule material and a nominal value of 3 cm for its height. All the rest are modeled quite accurately according to the parameters given.

The primary definer is a fixed opening made of tungsten. The adjustable collimator made of lead jaws is modeled as a continuous slab for the sake of computational simplicity. The trimmer bars are modeled as flat.

The Structure of Calculation

In the simulation of the full therapy unit we have split the calculation into two steps. In the first step 3×10^7 photons are initiated uniformly throughout the source material region and have an isotropic distribution. The output of the data reaching the scoring plane contains energy, position, direction and history for every particle. We simulated different openings of the outer collimator to get field size from 5×5 to $30 \times 30 \text{ cm}^2$ at SSD equal to 80 cm. Different thicknesses for the anti-scattering grid are simulated, as well as different material including lead, tungsten and depleted uranium.

In the second step, the electron mode was used. 10^6 photons were initiated uniformly throughout the source material region in a isotropic distribution. Instead of the 140-energy bin that was used in the first step, 14 were used in this step. Different thicknesses for the lead sheet were simulated.

Primary Spectrum Simulation of Cobalt-60 Machine

For primary photon spectrum simulation, it is noted that cylindrical symmetry exists, which is to the advantage of the simulation. The scoring cell is placed beneath the machine; the distance between the Cobalt-60 source and the scoring cell is 80cm. MCNP tally type 4 (photon flux) F4 is used. The simulated primary spectrum is shown in Figure 4-2.

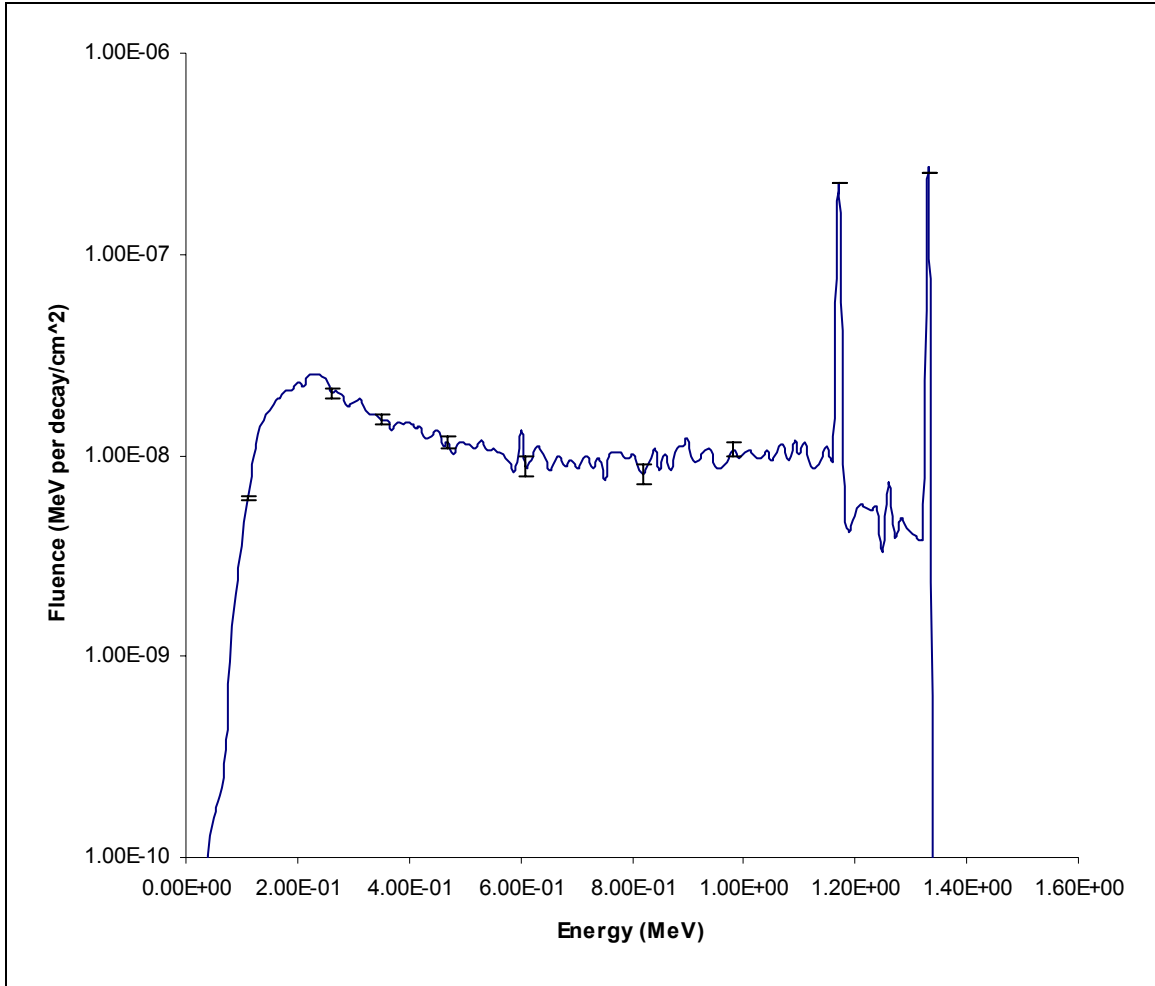


Figure 4-2. On-axis energy spectra of photons reaching the scoring plane from Cobalt-60 machine (uncertainty in the peak is less than 0.1%, in the tail is always less than 10 %).

Figure 4-2 shows the on-axis photon spectrum calculated for a broad beam ($30 \times 30 \text{ cm}^2$) at 80 cm SSD. As shown in this figure, there is a significant number of photons scattered from the lead shield and the other geometry around the source.

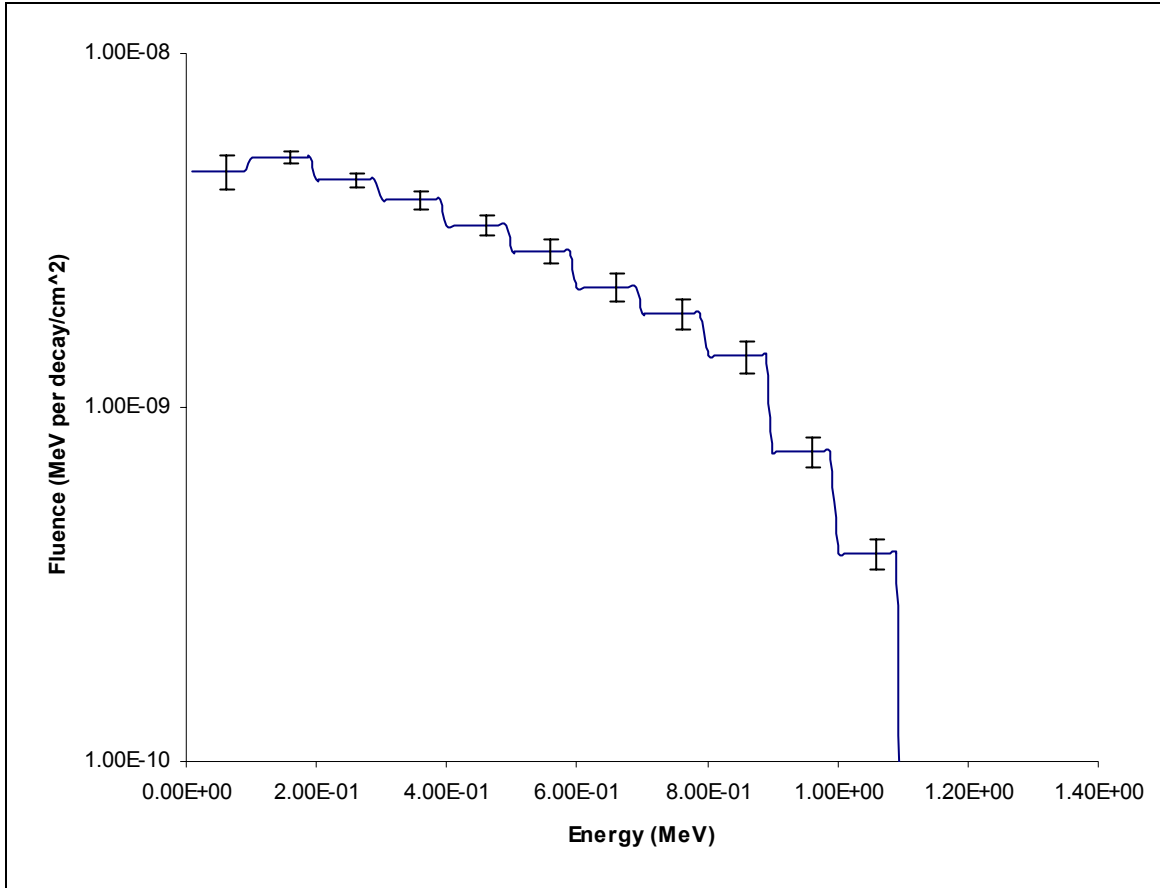


Figure 4-3. On-axis energy spectra of electrons reaching the scoring plane from Cobalt-60 machine. The spectrum is calculated for scoring region of $8 \times 8 \text{ cm}^2$ (uncertainty is less than 10 %).

The electron spectrum shown in Figure 4-3 is calculated for a larger region ($8 \times 8 \text{ cm}^2$ instead of $2 \times 2 \text{ cm}^2$ in the photon case) because of the poorer statistics. The average energy of electrons is about 380 keV. Although the electron fluence is a factor of about 100 less than the photon fluence even for the largest field, it must be remembered that the dose delivered per unit fluence of electrons is typically 100 times greater than for photons (16).

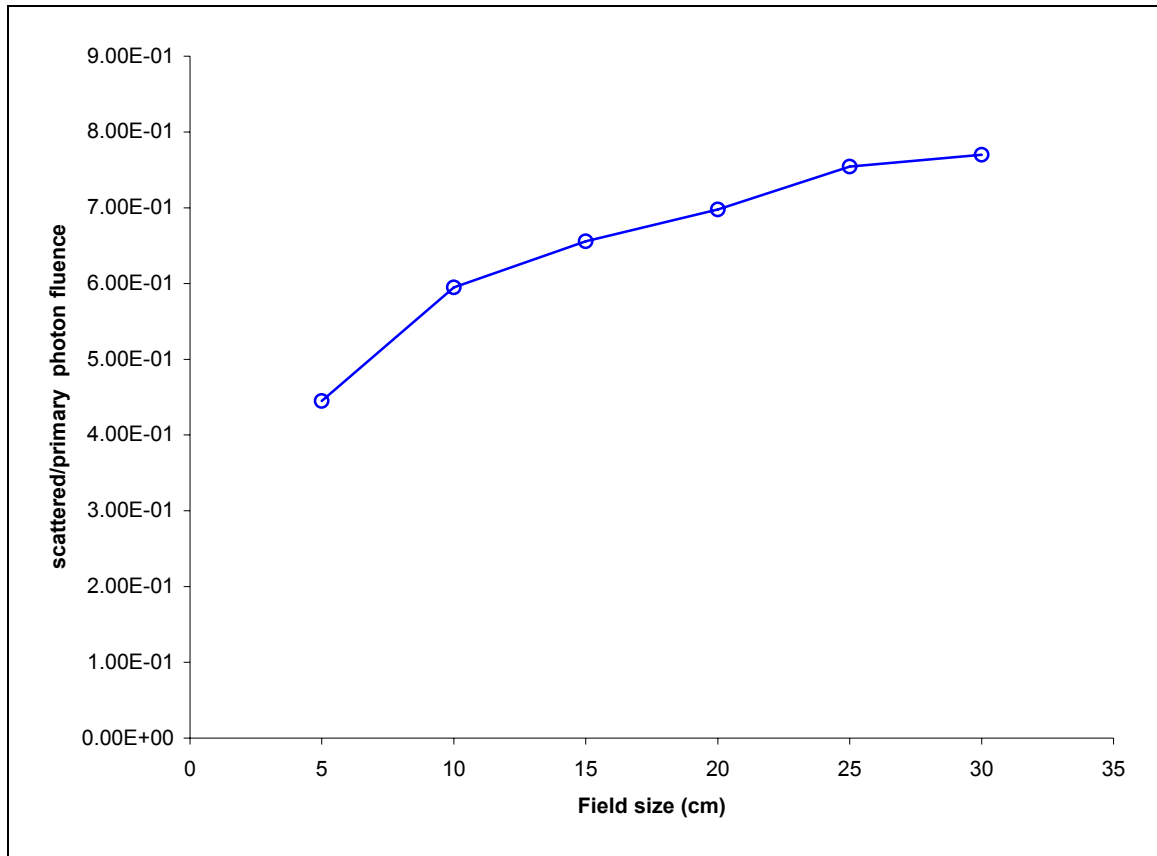


Figure 4-4. Photons fluence versus field size reaching a plane at SSD= 80cm. The fluence is scored in a $2 \times 2 \text{ cm}^2$ region on the axis.

Figure 4-4 shows the relative fluence of scattered to primary photons reaching a plane at SSD=80 cm versus field size. The ratio of photons scattered to primary increases as the field size increases, for a field size of $5 \times 5 \text{ cm}^2$ the ratio was about 0.42, while for a field size of $30 \times 30 \text{ cm}^2$ the ratio jumped to about 0.78.

The scattered photons from the source region include a component from the lead shield surrounding the source capsule which is a constant 25% of the total number of photons, except for the field sizes less than $10 \times 10 \text{ cm}^2$. For a field size of $5 \times 5 \text{ cm}^2$, the number of photons scattered from the collimation system represents about 5% reaching 80.5 cm SSD, while for a field size of $30 \times 30 \text{ cm}^2$, the contribution is equal to 15% from

the primary and adjustable collimator. This scatter explains the observed variation of the ratio of photons scattered with field size and is qualitatively consistent with field size.

Filtered Spectrum Simulation of Cobalt-60 Machine

The on-axis photon energy spectra shown in Figure 4-5 are calculated in the $2 \times 2 \text{ cm}^2$ region. The figure compares the photon spectra for five different cases; with no grid, 2.5 cm, 5 cm, 7.5 cm and 10 cm thicknesses; cases are represented in Figure 4-5

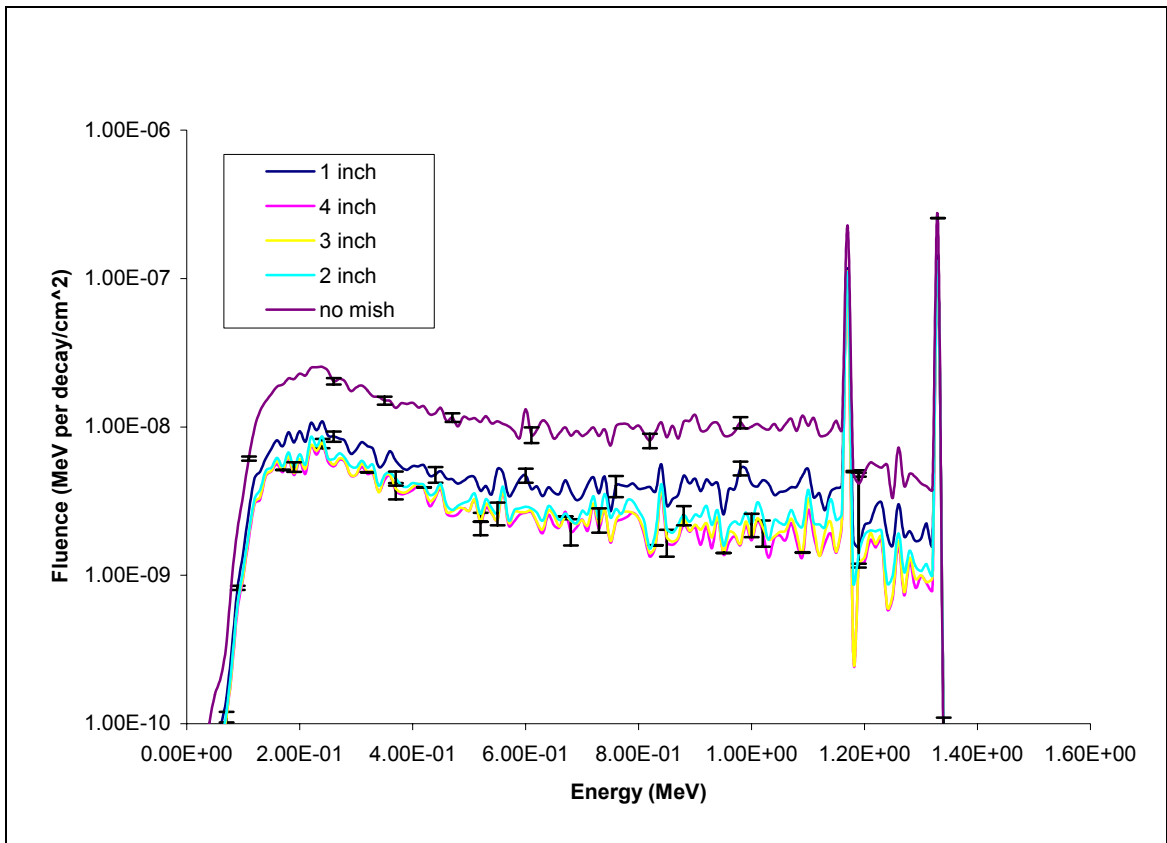


Figure 4-5. On-axis energy spectra of photons reaching the scoring plane from Cobalt-60 machine (uncertainty in the peak is less than 0.1%, in the tail is always less than 10 %).

It is clear from the Figure that using thicker anti-scattering grid filters out the scattered radiation more effectively than thinner ones. This can be explained in that the

higher probability of scattered radiation to be attenuated in more than one septal is greater. However, the 7.5 cm and 10 cm thickness grid did not reduce the scattered photons significantly more than 5 cm.

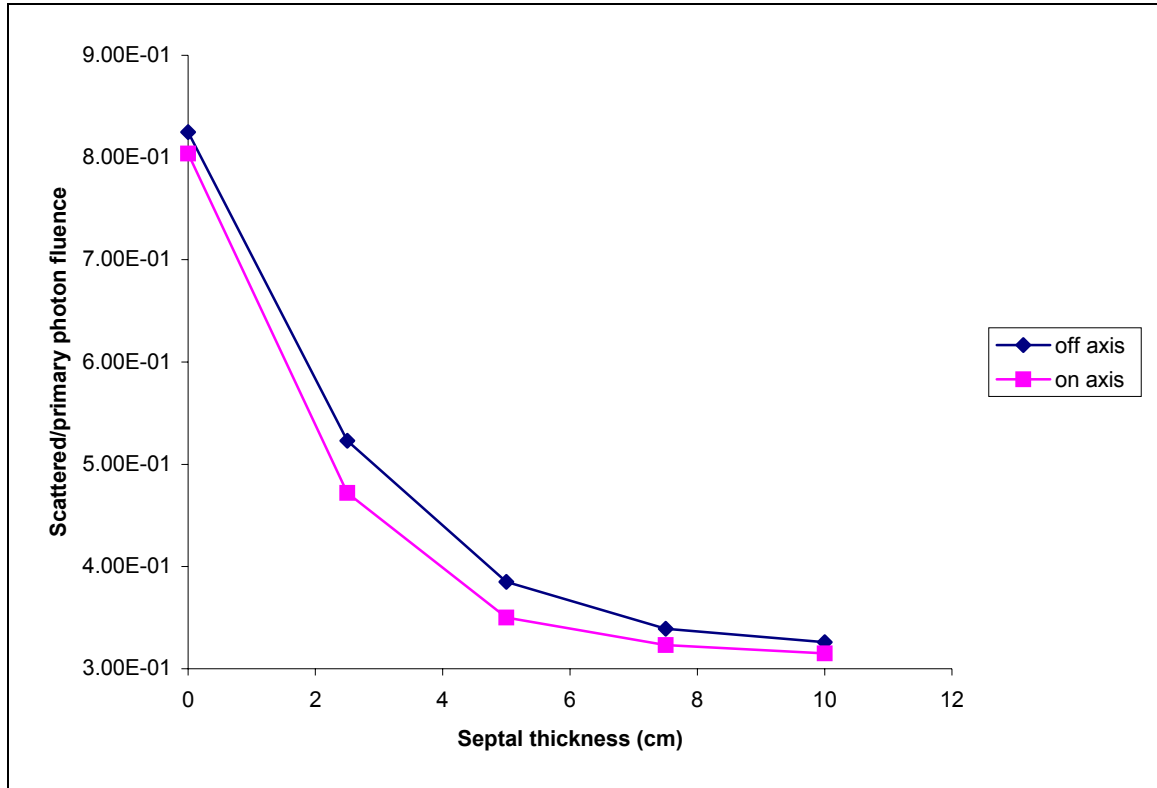


Figure 4-6. On axis and off axis scattered to primary photons fluence ratio versus septal thickness at SSD= 80cm. The fluence is scored in a $2 \times 2 \text{ cm}^2$ region.

Both off-axis and on-axis scattered to primary photon fluence ratio were compared in Figure 4-6. It is clear that for both cases scattered photon to primary ratio was reduced significantly when the anti-scattering grid was used. However, that ratio is higher for the off-axis case.

Different numbers of septa were also compared including grids of 11, 21 and 41 septa. The length of the septa is set to be 5 cm. The 11 septa grid did not reduce the scattered photons; on the contrary, the percentage of scattered radiation increased. This

can be explained by the existence of big holes that this grid has that allows the scattered radiation to penetrate, and some primary photons to be scattered from the grid itself. On the other hand, grid two (21 and 41 septa) reduced the scattered photons fluence significantly by 40%.

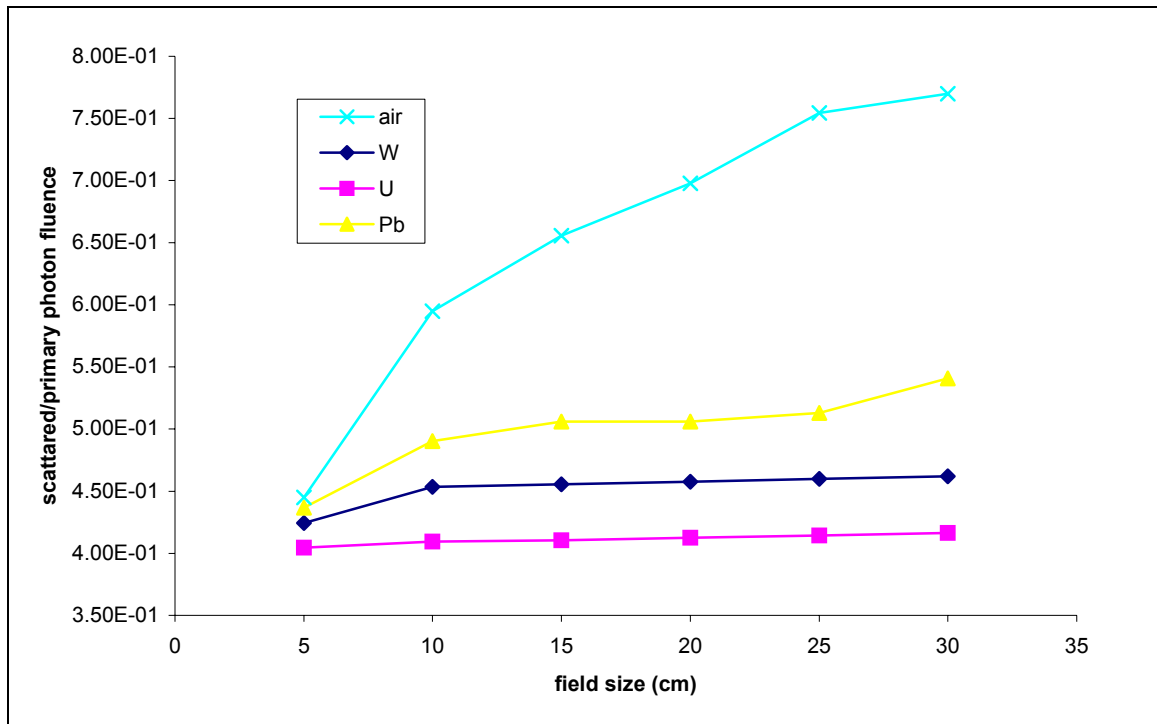


Figure 4-7. Photons fluence versus field size reaching a plane at SSD= 80cm. The fluence is scored in a $2 \times 2 \text{ cm}^2$ region on the axis.

Figure 4-7 shows the relative fluence of scattered to primary photons reaching a plane at SSD=80 cm versus field size for different material. On the contrary, in the unfiltered spectrum, the ratio of photons scattered to primary remains almost constant for the filtered one as the field size increases. Also, it is very clear that the percentage of scattered to primary photons is significantly lower for the filtered spectrum as well.

The fluence of scattered photons, which has the highest impact on dose in the buildup region, is significantly lower than the unfiltered for all cases below the 511 keV peak. The corresponding values in terms of energy fluence are 15, 17 and 24 % of the scattered radiation, respectively, for depleted uranium, tungsten and lead, which results in significant reduction in the dose to the skin.

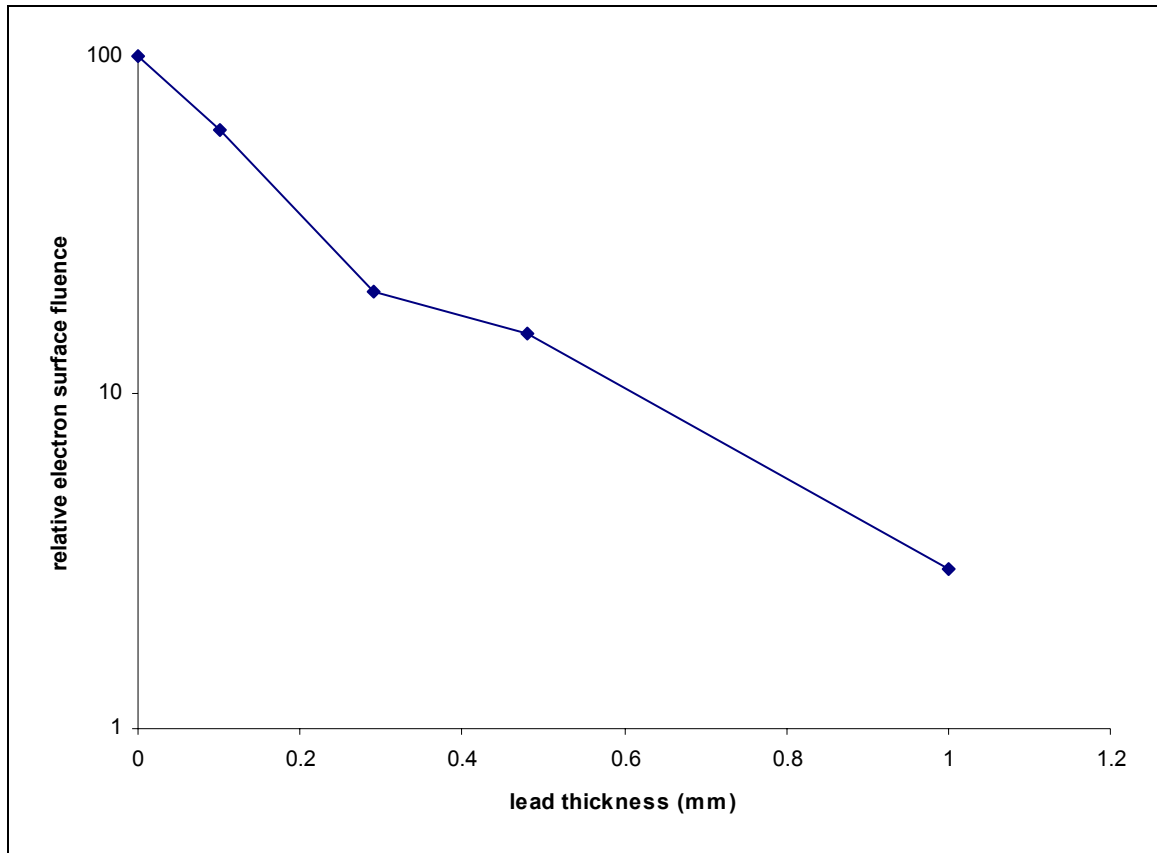


Figure 4-8. Electron relative fluence reaching a plane at SSD= 80cm versus lead filter thickness. The number of electrons is normalized to the total photon fluence. The fluence is scored in a $8 \times 8 \text{ cm}^2$ region on the axis.

To see how effectively the filter removes the upstream electrons, we have performed calculations for electron beam traversing various lead filters and the air past the filters. Figure 4-8 plots the relative electron fluence versus the thickness of the lead

filter. It is shown from Figure 4-8 that a 1mm lead filter reduces the contamination electron fluence to a few percent or less of its unfiltered value.

The Effect of the Lead Filter on Photon Beam Quality

The present calculations show that the lead filter slightly hardens the photon spectra. The percentage of photons fluence of energies greater than 1 MeV increases by up to 1% compared to its unfiltered value. For a precise determination of clinical beam quality index, this photon filtering effect should be taken into account.

The Effect of the Anti-Scattering Grid on Photon Beam Quality

A drawback that might arise from the anti-scattering grid is the inhomogeneity that caused by the septa of the grid. The presence of any object in the path of the radiation will cause a “shadow”, causing lower values of dose to be delivered to regions beneath. Using a higher number of septa with smaller thicknesses can solve such an obstacle. At the same time, this allows the scattered radiation to be absorbed by more than one septal without affect the attenuation properties.

CHAPTER 5 EXPERIMENTAL SETUP

While the knowledge about the spectral information from Cobalt-60 therapy machines is fundamental in such an application, how to get the information presents a daunting task. The difficulty lies in the fact that the detector is in an intense field with billions of particles bombarding it, and will be saturated instantly. In addition, the detecting efficiency falls off drastically at high energy. To remedy this saturation, an experiment based on the scattering method is designed. The scattering method can effectively reduce the high intensity and the energy spectrum is shifted to lower energy range. However, in applying this method to a practical situation, attention should be paid in setting up the components of the experiment.

An experiment was designed to check the output of the MCNP simulation. This experiment was based on the incoherent scattering spectroscopy (ISS) and to be used in future studies to benchmark and validate the results from the Monte Carlo simulation. In this method, a small scattering material is put in the beam, and the once-scattered spectrum is then measured at a certain angle, so that from the scattered spectrum it is relatively simple to deduce the original spectrum. The scattered radiation intensity incident on the detector is reduced by several magnitudes by the scattering process; furthermore, the energy of the scattered photons is reduced as well because of the incoherent scattering, so that a more suitable energy range for the detector is obtained.

A drawback of the incoherent scattering method is that higher energy photons have a smaller probability of being scattered than do lower energy photons. Also, they suffer a greater fractional decrease in their energy on incoherent scattering; this method results in a reduction of resolution. To demonstrate this effect quantitatively, a mono-energetic source and a spectrometer with good spectral resolution are needed. Also, in the incoherent scattering method, it is necessary to define an accurate scattering angle. This procedure needs a collimator, which not only causes distortion in measured spectrum, but also increases the difficulty in alignment.

Choice of Scattering Angle

The scattered photon energy after the scattering process is given by the Compton energy-angle relation:

$$E = \frac{E_0}{1 + \frac{E_0}{m_0 c^2} (1 - \cos \theta)} . \quad (5-1)$$

As the incident energy becomes very large compared with the rest mass energy, the electron Eq.(5-1), can be approximated by:

$$E = \frac{m_0 c^2}{1 - \cos \theta} . \quad (5-2)$$

For a scattering angle of 30° the scattering photon range is between 0 and 3.8 MeV; for a scattering angle of 60° the scattering photon energy range is between 0 and 1.022 MeV; and for a scattering angle of 90° the scattered photon energy range is between 0 and 0.511 MeV. Thus we can see that the incoherent scattering process squeezes the original spectrum to a narrow range; this “shrinkage effect” is more evident

with larger scattering angles. To minimize the effect, a smaller angle is preferred. On the other hand, detector calibration and detecting efficiency considerations include:

- Suitable gamma source for detector efficiency calibration are not available for higher energies;
- ◆ The detector efficiency of germanium spectrometers decreases rather rapidly for photons of energy above a few MeVs.

Because of these two conflicting requirements, a compromise must be reached.

With the use of Eq. (5-1), the scattering angle that yields a maximum energy can be calculated as follows:

$$\cos \theta = 1 + \frac{m_0 c^2}{E_0} - \frac{m_0 c^2}{E}, \quad (5-3)$$

where the E_0 is the end point energy of the spectrum, and E is the upper limit of the scattered spectrum. For preliminary analysis, E assumes a value of 2 MeV, 1.5 MeV, 1.0 MeV and 0.511 MeV, respectively. The calculated results are shown in Figure 5-1.

Effects of Collimator

A collimator is used in front of the detector to define the scattering angle. The collimator effects the detected energy spectrum in two ways. The first one is the buildup effect, which is dependent on the material that the collimator is made of and the incident spectrum. The secondary photons (including degraded photons, bremsstrahlung photons and characteristic x-rays) from the edge of the collimator will deform the incident spectrum.

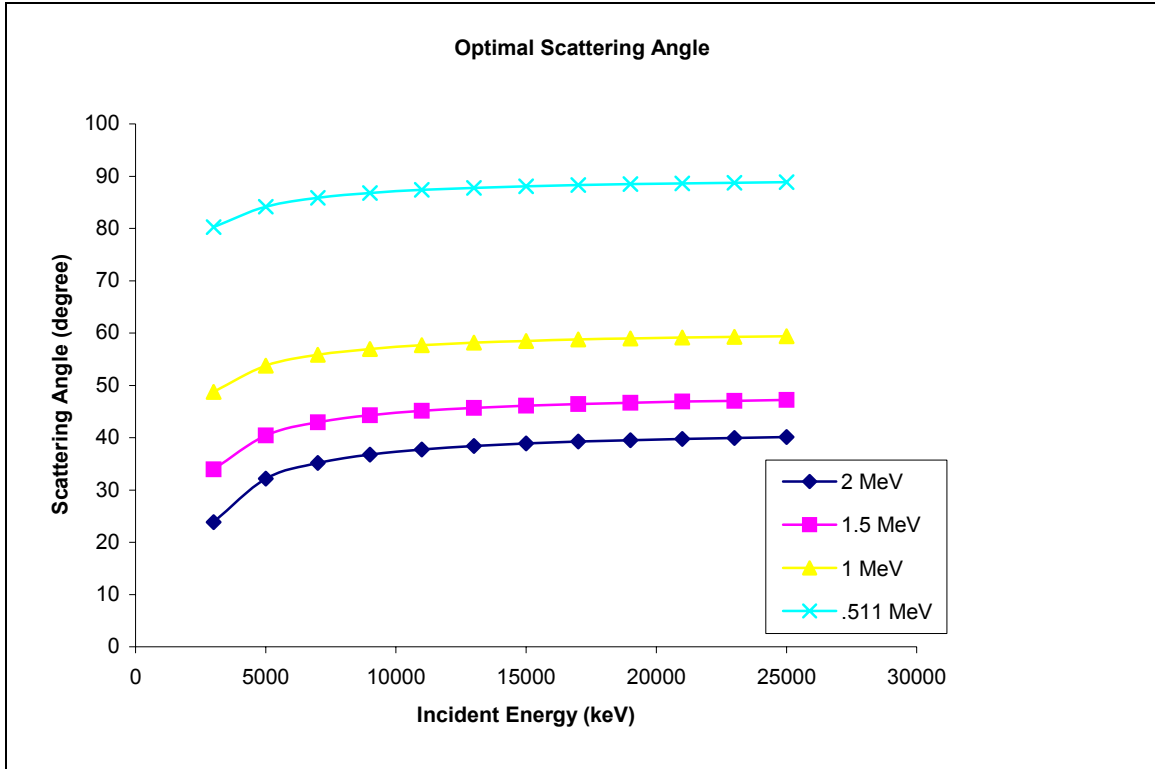


Figure 5-1. Optimal scattering angle for different detecting scattered energy ranges and incident photon energy.

Because this effect is difficult to demonstrate analytically, the Monte Carlo technique is a good method to show the effect directly. The second thing that the collimator affects is the scattering angle. To make the scattering angle as accurate as possible, the radius of the pinhole in the collimator should be as small as possible. In practice, the pinhole is of finite size, causing the scattered photons to have a small spread in their energies. This is defined as the geometric line-broadening effect. The severity of this effect can be calculated with the aid of differentiation of the Compton energy-angle relation:

$$dE = \frac{m_o c^2}{\left[1 + \frac{m_o c^2}{E_o} - \cos \theta\right]^2} d(\cos \theta).$$

(5-4)

The results are shown in Figures 5-2, 5-3 and 5-4, for monoenergetic photons with energies of 100 keV, 1 MeV and 10 MeV respectively at different scattering angles.

The geometric line broadening of the scattered spectrum due to the deviation of the scattering angle can be significant. Care should be taken in actual experiments to make sure that the deviation from the specified scattering angle is minimized.

The choice of the collimator material, which is discussed in the next section, follows essentially the same principles that were required for shielding material. Depending on the actual situation, the design of the collimator is also important.

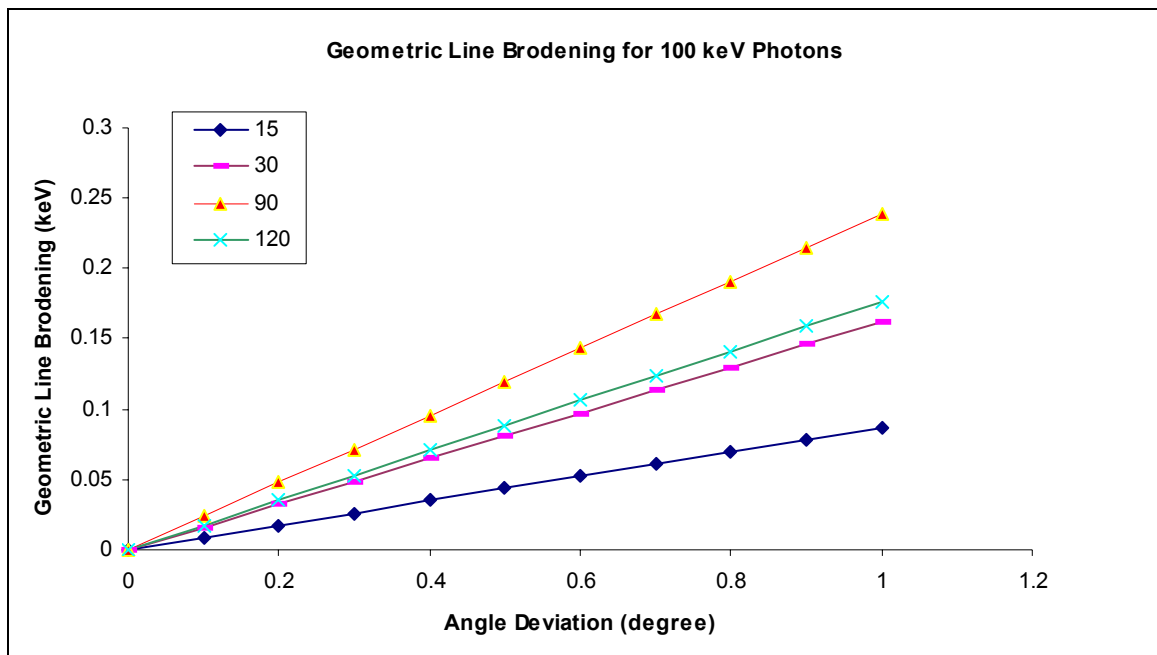


Figure 5-2. Geometric line broadening for 100 keV photons.

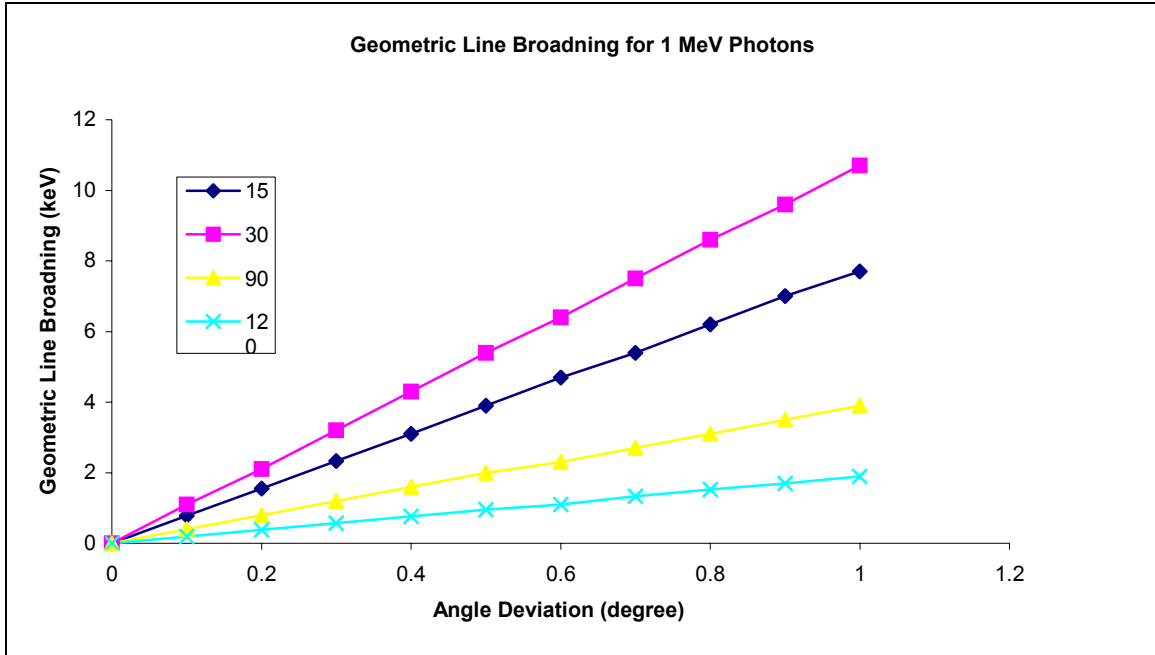


Figure 5-3. Geometric line broadening for 1000 keV photons.

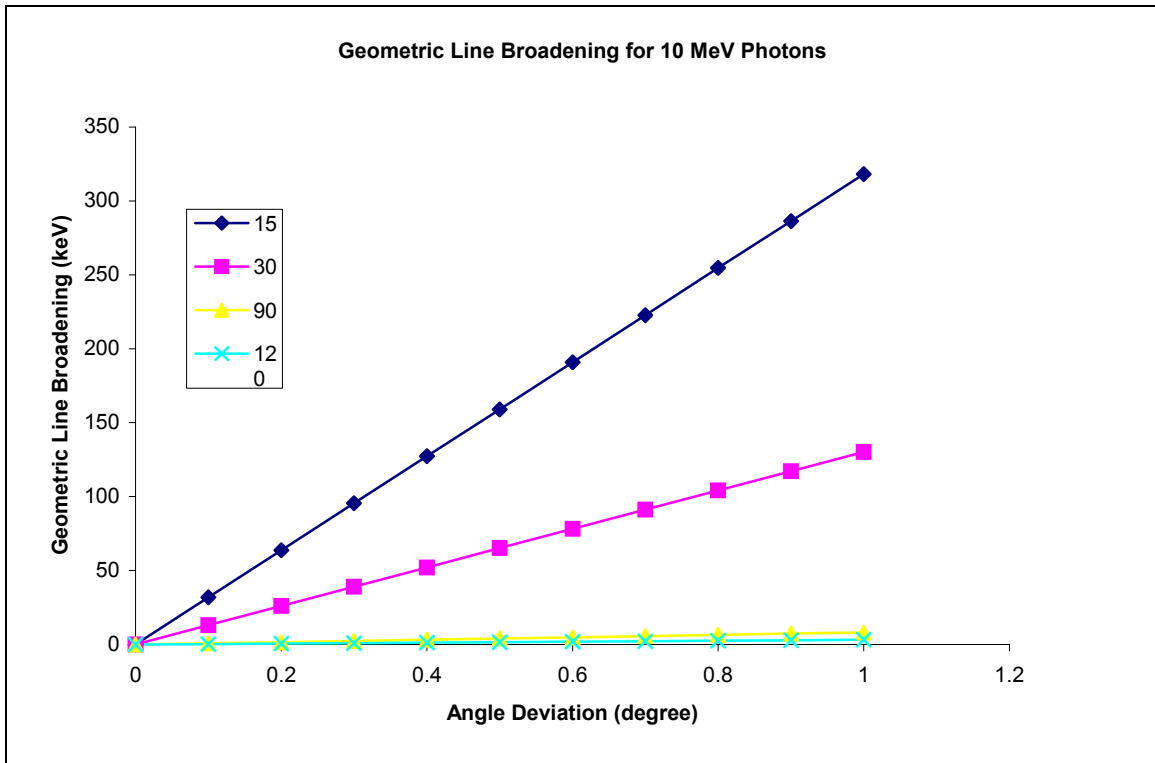


Figure 5-4. Geometric line broadening for 10 MeV photons.

Choice of Shielding Material

Shielding material are needed for both photons and neutrons. The commonly used photon shielding material is lead, the cross section of which is shown in Figure 5-5. From Figure 5-5 we observe that below 0.4 MeV the predominant mode of interaction is the photoelectric effect, which means if the primary photon energy is degraded to below 0.4 MeV, there is an almost certain likelihood that photons will be absorbed, generating x-rays. These characteristic x-rays, even if they can make it to the detector, can be distinguished easily causing little complication. Depending on the photon energy, the required thickness of lead can be readily estimated.

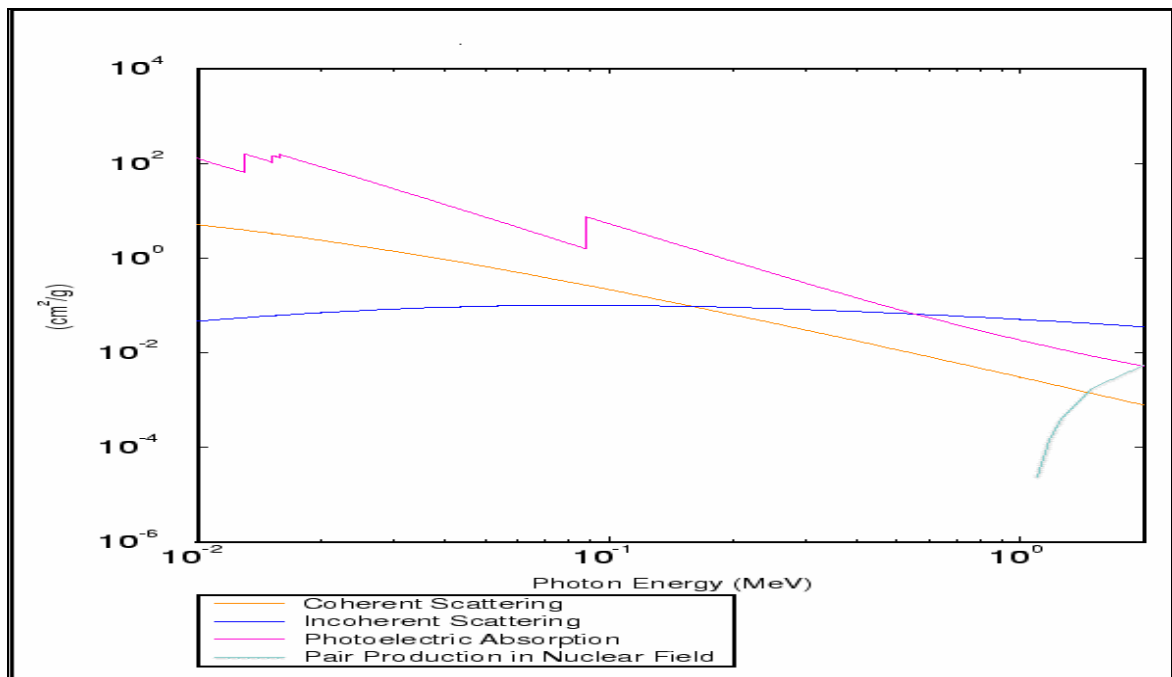


Figure 5-5. The photon cross sections for lead.

Photoneutrons generated by (γ, n) reactions in a high energy x-ray radiation field can be annoying, and proper attenuation should be paid to eliminate their effect. Neutrons are known to activate not only Ge crystal in the detector, but surrounding material as

well, complicating the response of the spectrometer. The induced radioactivity can cause severe pileup problems in some cases.

Choice of Scattering Material

Ideally, from Eq. (2-4), we would like to have only incoherent scattering so that the process of deducing the original spectrum is easier. This condition can be met at high energies and large scattering angles. For low Z material, Compton scattering is a very good approximation of incoherent scattering under the above-mentioned conditions. This approximation greatly simplifies the process, as the atomic number Z can be used to replace the incoherent scattering function $S(x, Z)$, the Compton energy-angle relation can be used to deduce the energy and the well-known Klein-Nishina formula can be used to obtain the differential probability. Usually the Compton scattering cross section in low Z material at high energies is large, which makes them very suitable for scattering purposes. When using carbon, the Compton process is predominant for photon energies between several hundred keV up to a few MeV. The photoelectric effect in this energy range is negligible, and pair production amounts to only a small percent of the total cross section. The photon differential atomic coherent and incoherent scattering cross sections for several scattering angles with three different energies are shown in Figures 5-6, 5-7 and 5-8. In comparison, the photon differential cross sections for lead under the same conditions are shown in Figures 5-9, 5-10 and 5-11. These data clearly show the advantage of low Z material as scatterers, if Compton scattering is desired.

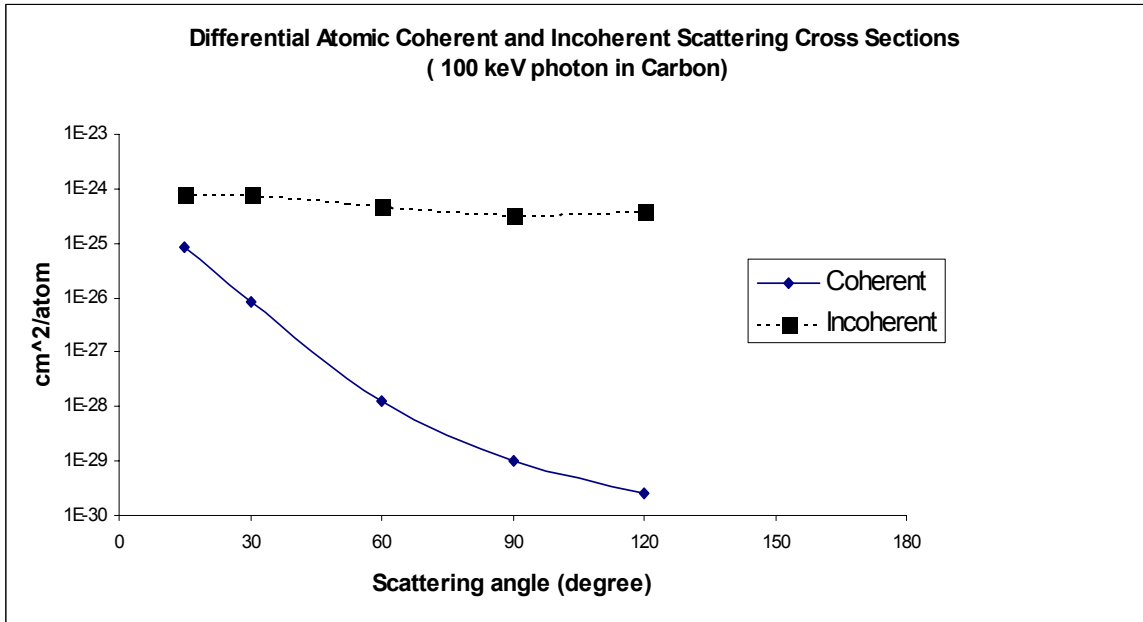


Figure 5-6. Differential atomic coherent and incoherent cross sections for 100 keV photons in carbon.

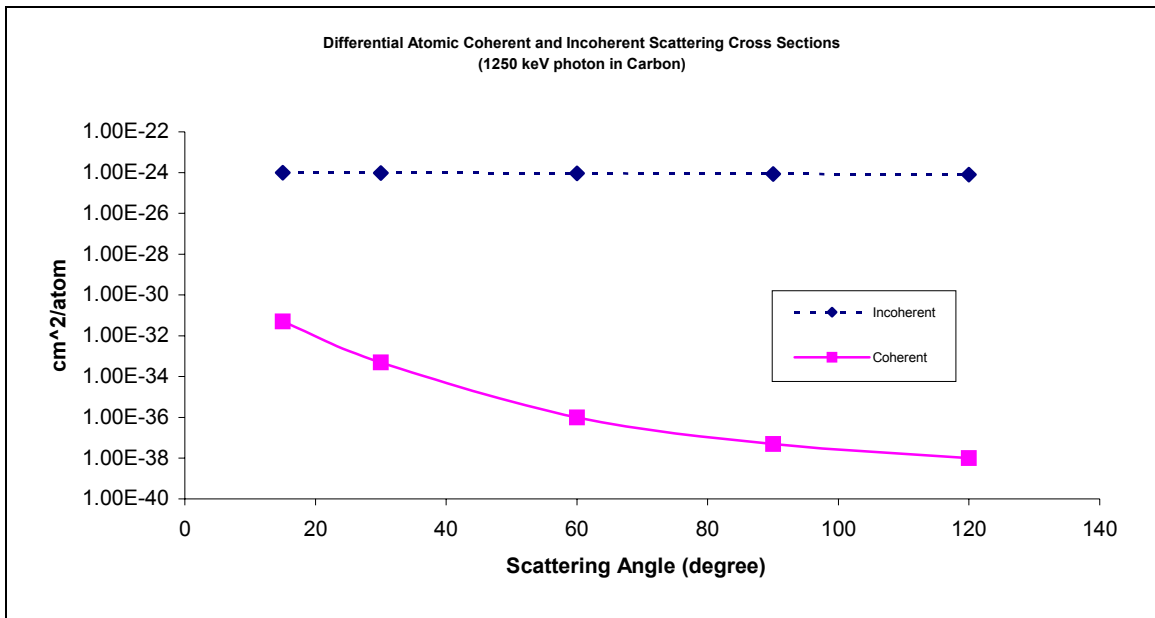


Figure 5-7. Differential atomic coherent and incoherent cross section for 1250 Kev photons in carbon.

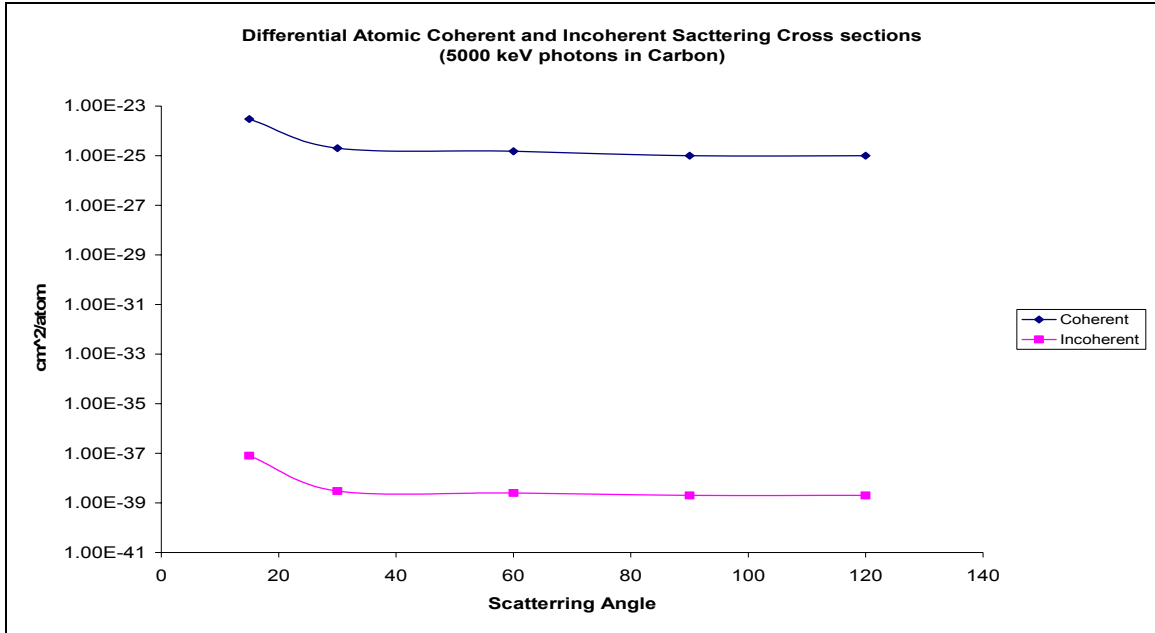


Figure 5-8. Differential atomic coherent and incoherent cross sections for 5000 keV photons in carbon.

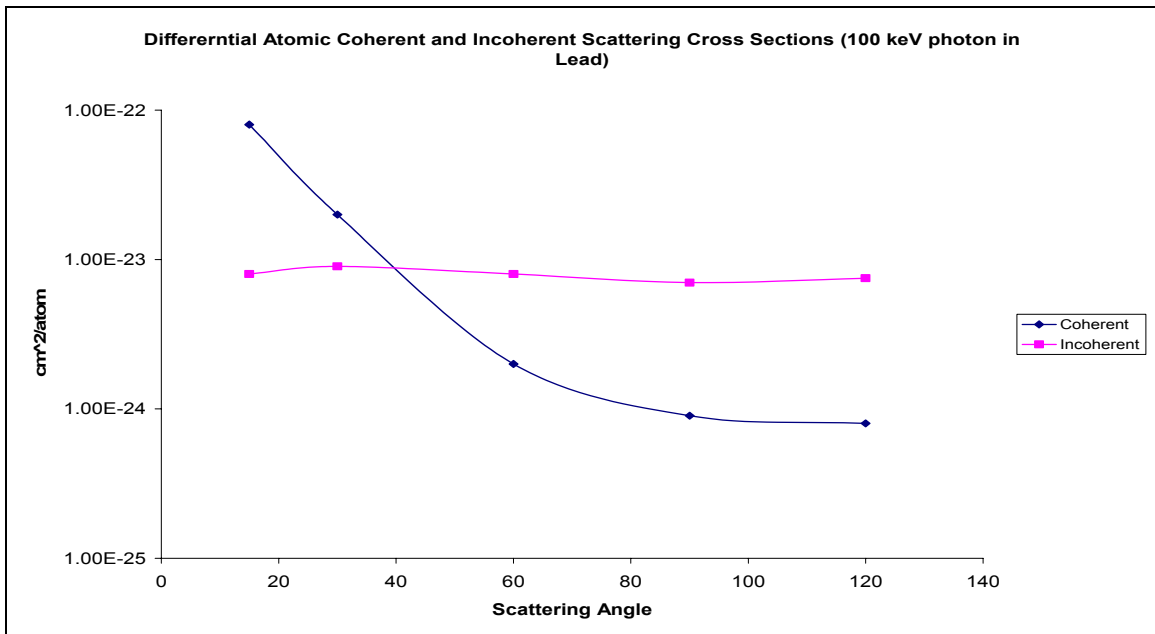


Figure 5-9. Differential atomic coherent and incoherent cross sections for 100 keV photon in lead.

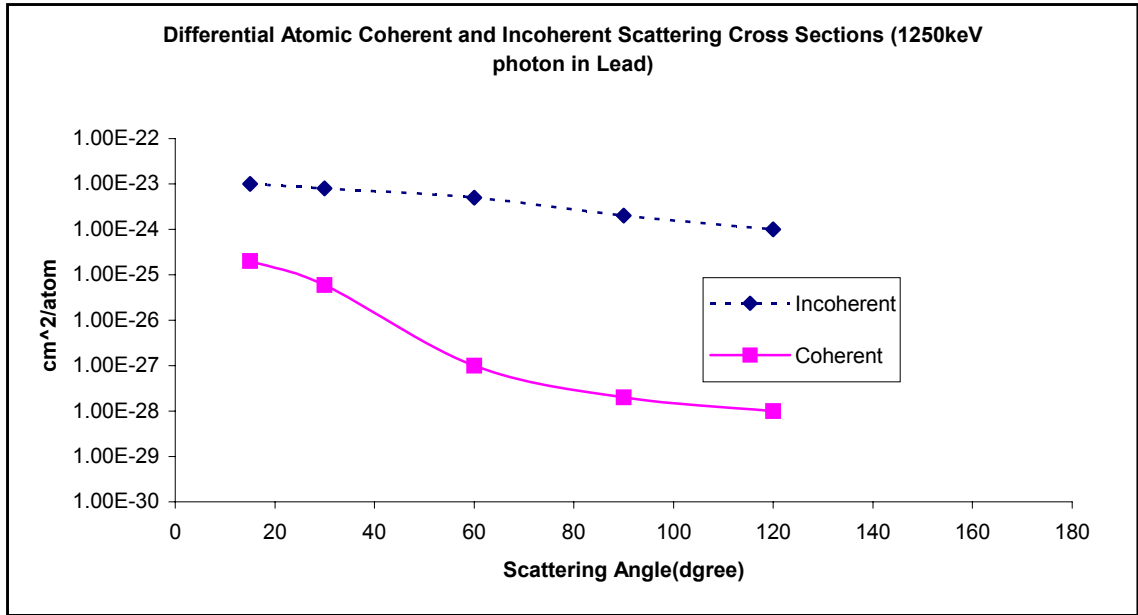


Figure 5-10. Differential atomic coherent and incoherent cross sections for 1250 keV photons in lead.

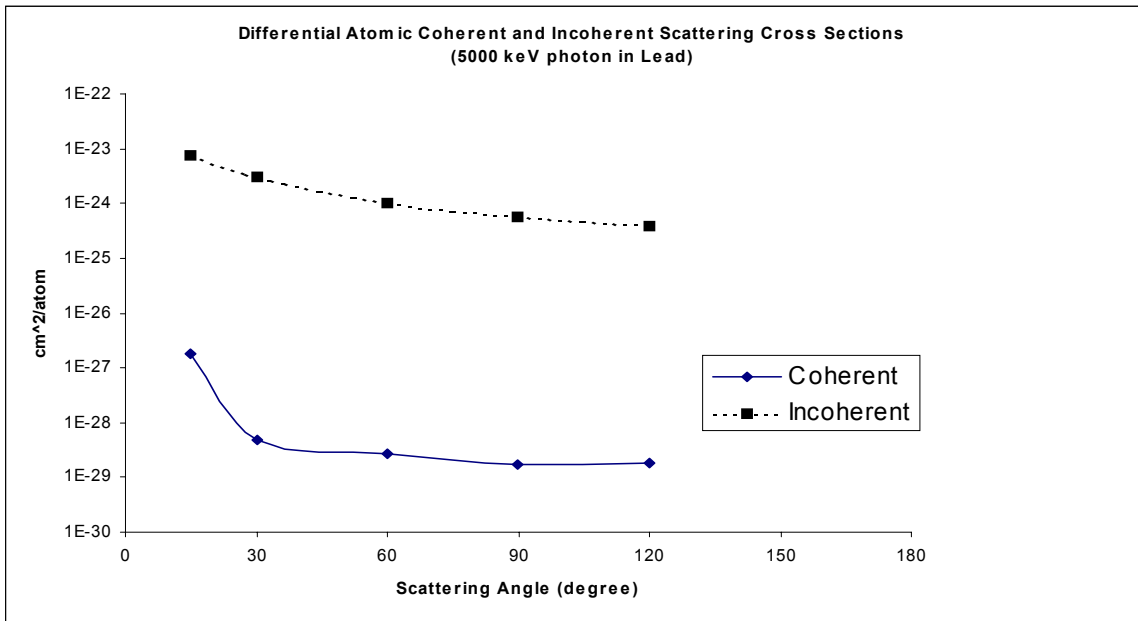


Figure 5-11. Differential atomic coherent and incoherent cross sections for 5000 keV photon in lead.

Cobalt-60 Therapy Machine

A typical Cobalt-60 machine consists of the following:

1. an encapsulated radioactive source,
2. a source shielding or housing,
3. a shutter device to turn the beam on and off,
4. a collimating system to limit the size of the beam,
5. a support mechanism by which the beam can be oriented with respect to the volume to be treated, and
6. an ancillary device attached to the source shield or the support mechanism to facilitate beam alignment or other clinical procedures.

Cobalt is a brittle, hard ferromagnetic metal having an atomic weight of 58.94, a density of 8.9 g/cm^3 and the atomic number 27. Cobalt-60 can be readily produced by neutron irradiation of Cobalt-59 in a nuclear reactor. It is known that the attainable specific activity is strongly dependent upon neutron flux. Efficient production of high-specific activity sources for Cobalt-60 teletherapy can be achieved only in reactor positions in which the flux is 10^{13} neutrons per square centimeter per second or higher.

Cobalt-60 decays to Nickel-60 with the emission of beta particles with a maximum energy 0.32 MeV and two photons per disintegration of energies 1.172 and 1.332 MeV. Sources today are made of nickel-cobalt alloy to eliminate dusting and corrosion. These high-specific activity pellets are doubly encapsulated. Both inner and outer capsules are made of low carbon stainless steel and are sealed by heliarc welding. This kind of encapsulation enables the production of 1.5 cm and 2.0 cm sources with outputs to 250 R/min at 1 meter (Rmm). The beta particles are absorbed in the cobalt and nickel metal, and the resulting capsules emit bremsstrahlung x-rays and a small amount of

characteristic x-rays. These low energy x-rays are strongly attenuated, and do not contribute appreciably to the dose in the patient.

The shielding of the high-specific activity becomes important to ensure that the source is placed in a safe condition (i.e., with the shutter closed). Conservatively, the leakage radiation from the source shielding will average less than 2 mR/hr at a distance of 1 meter from the source in all directions, and will at no time exceed 10 mR/hr at this distance. For a source at the kilocurie range of activity, this requires an attenuation factor of about 10^6 , or approximately 20 half-value thickness (HVT).

A shutter is a general term describing the means by which the useful beam of radiation can be interrupted. It is imperative that in the event of power failure the unit immediately returns to the “off” position. An auxiliary safety feature, which should be included, is a means by which manual closing of the shutter is possible.

An integral part of the shutter system is the timing device that terminates the exposure. Since the dose rate can be determined to a high degree of precision for any set of treatment conditions, the exposure time is the all-important parameter in treatment. The timer must be accurate and unfailing in its operation, and must be designed so as to minimize “operator error”.

The Collimation System

The purpose of the collimating system is to permit the useful beam to be shaped to fit the treatment volume. To be practical, a collimator should be designed to permit all possible rectangular fields from $4 \times 4 \text{ cm}^2$ to $35 \times 35 \text{ cm}^2$. In addition, complex fields shaped for the individual patient, by the use of additional shielding blocks placed on a tray under the collimator, are also needed. The simplest form of continuously

adjustable diaphragm consists of two pairs of heavy metal blocks. Each pair can be moved independently, so as to be able to obtain a square or a rectangular-shaped field. Some collimators are multi-vane type. In either case, the radiation will pass through the edge of the collimating blocks, resulting in what is known as the transmission penumbra and secondary interactions, which produces scattered photons and electrons. It is now known that the collimating system is the main reason for the heterogeneity of the radiation beam from a Cobalt-60 machine.

High Purity Germanium Detector

In gamma ray spectroscopy, greater detector volume is preferred for two reasons. First, by using a larger detector the response function can be simpler, and second, higher energy gamma rays can be detected with greater efficiency. One approach taken to achieve large detector volume is to reduce the impurity concentration. Techniques have been developed to reduce the impurity concentration to approximately 10^{10} atoms/ cm^3 in germanium. Detectors that are manufactured from this ultra-pure germanium are called high-purity germanium (HPGe) detectors. The HPGe detectors can have either planar or coaxial configuration. Because of the small band-gap (0.7 eV), room-temperature operation of germanium of any type is impossible because of the large thermally-induced leakage current that would result. Instead, germanium detectors must be cooled, and normally an insulated dewar, in which a reservoir of liquid nitrogen is used, is in thermal contact with the detector.

The high-purity germanium detector (HPGe) has the advantages of excellent energy resolution, high detecting efficiency and ease of use. The diameter of the Ge crystal is 5.0 cm and the thickness is also 5.0 cm. The aluminum thickness is 1.27 mm. The detector

operates at a positive 2500 V bias. The measured full width at half-maximum (FWHM) resolution of the detector and the electronics is about 1.6 keV at 1330 keV. The relative efficiency at this energy is about 13%; the peak to Compton ratio is around 40%.

Electronics

The output from a gamma ray detector is, in essence, an amount of electrical charge proportionate to the amount of gamma ray energy absorbed by the detector. The function of the electronic system is to collect charge, measure the amount and store the information.

A typical simple electronic system for gamma ray spectrometer is shown in Figure 5-12. The bias supply provides the electric field to sweep the electron-hole pairs out of the detector, which are then collected by the preamplifier.

The collected charge is then converted to a voltage pulse. The linear amplifier changes the pulse shape and increases its size. The Multi Channel Analyzer (MCA) sorts the pulses by pulse height, and counts the number of pulses within individual pulse height intervals. In modern systems, the detector and the preamplifier are manufactured as a unit; the first stage of the preamplifier is intimately attached to the detector capsule. This arrangement has advantages in that critical components of the preamplifier can be cooled to reduce thermal noise.

More often the other items in the system that includes the MCA are purchased in the Nuclear Instrumentation Module (NIM) modular format. NIM modules are manufactured to standard physical dimensions and fit into a “slot” in a NIM-bin, which contains standard electrical power supplies. The NIM standard also defines the pulse and logic specifications for the signals passing between modules. In this way, it is possible to

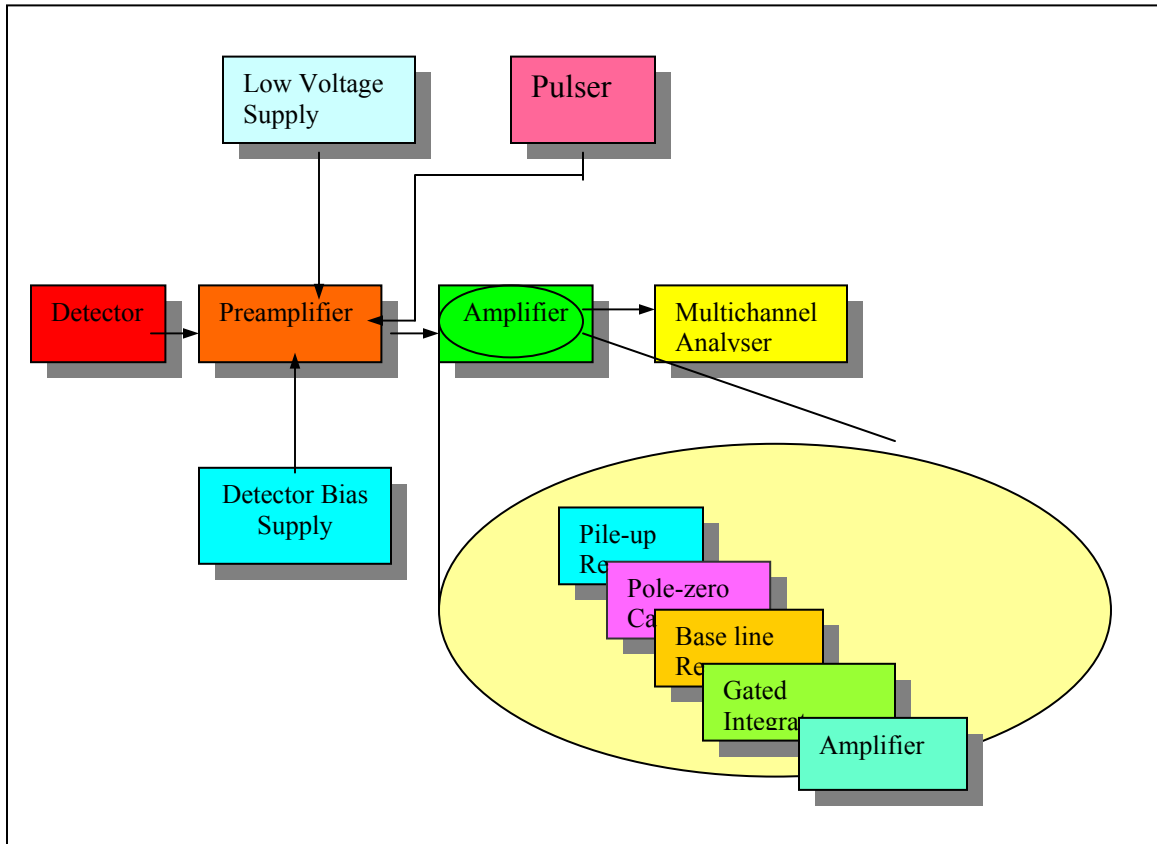


Figure 5-12. A schematic electronic system for gamma spectroscopy.

install a variety of modules from different manufacturers within the same bin, and for them to work together as part of a complete system.

A NIM bin is used to accommodate the power supply for the detector, amplifier and spectrum master. Pulses from the detector is amplified and shaped with 2 microseconds differentiating time constant and applied to a 16834-channel pulse-height analyzer (multi channel analyzer, MCA). A calibration of pulse height versus photon energy for the spectrometer is to be performed using ^{241}Am , ^{137}Cs , and ^{60}Co or other available sources. A linear curve representing the relation between the pulse height and the photon energy is then to be obtained. Pulse pileup rejection, baseline restorer and

pulse shaping function is to be adjusted to optimize the operating condition of the spectrometer.

Detector Response

There are various ways gamma rays can interact in matter, however, only three interaction mechanisms have any significance in gamma ray spectroscopy; photoelectric absorption, Compton scattering and pair production. The effect of photoelectric absorption is the liberation of photoelectrons, which carries off most of the gamma ray energy together with one or more low-energy electrons corresponding to the absorption of the original binding energy of the photoelectron. If nothing escapes from the detector, then the sum of the kinetic energies of the electrons that are created must be equal to the original energy of the gamma ray photons. Photoelectric absorption is therefore an ideal process, if one is interested in measuring the energy of the original gamma rays. The total electron kinetic energy equals the incident gamma ray energy and will always be the same if monoenergetic gamma rays are involved. The result of a Compton scattering interaction is the creation of a recoil electron and scattered gamma ray photon, with the division of energy between the two depending on the scattering angle. In normal circumstances, all scattering angles will occur in the detector. Therefore, a continuum of energies can be transferred to the electron, ranging from zero up to the maximum recoil energy, which occurs at 180° . The pair production occurs in the Coulomb field of a nucleus or an electron of the absorbing material, and corresponds to the creation of an electron-positron pair at the point of complete disappearance of the incident gamma ray photon. Because energy of two times the rest mass energy of an electron is required to create the electron-positron pair, minimum gamma ray energy of 1.022 MeV is required

to make the process energetically possible. If the incident gamma ray energy exceeds this value, the excess energy appears in the form of kinetic energy shared by the electron-positron pair. A plot of the total (electron + positron) charged particle kinetic energy created by the incident gamma ray is a simple delta function, only 1.022 MeV below the incident gamma ray energy. The pair production is complicated by the fact that the positron is not stable. Once its kinetic energy becomes very low (comparable to the thermal energy of normal electrons in the absorbing material), the positron will annihilate or combine with a normal electron in the absorbing medium. At this point, both disappear and are replaced by two annihilation photons of energy of 0.511 MeV each.

As discussed above, the preferred mode of interaction is photoelectric absorption in gamma ray spectroscopy with monoenergetic energy peaks. However, the predominant interaction mode of germanium in the energy range of 0.2 to 2.0 MeV is Compton scattering. Because the ratio of the Compton scattering to the photoelectric cross section is large, a much greater fraction of all detected events lies within the continuum rather than under the photopeak.

In a normal detector, the measured spectrum consists of a photopeak (full energy deposition), a Compton edge, a Compton continuum and the continuum between photopeak and Compton edge, which is due to multiple Compton scattering. If the energy is high enough to make pair production occur, a single escape peak and /or double escape peak will be observed. Other complications include escape of secondary electrons, escape of bremsstrahlung and escape of characteristic x-rays. Sometimes the surrounding material near the detector will have an influence on the observed spectrum in the form of

back-scattered peak, annihilation peak or characteristic x-ray peak. Summation peaks can also be seen occasionally.

For the usual geometry in which the gamma rays are incident externally on the surface of the detector, interaction taking place near the surface of the detector will have a larger probability of partially losing energies, thus complicating the response function. The response function to be expected for a real gamma ray detector will depend on the size, shape and composition of the detector, and also on the geometry details of the irradiation conditions.

The discussion above is only applicable to monoenergetic photons. For x-rays with a certain spectrum, the response function of the detector is more complicated, and can only be adequately predicted by using the Monte Carlo method.

Experimental Setup

The detecting system employed in this experiment is shown schematically in Figure 5-2. The HPGe detector first is placed at about 150 cm away from the beam axis of the Cobalt-60 unit. The lead shielding surrounding the HPGe detector has to be thick enough to stop scattered radiation in different angles from reaching the detector. Radiation is admitted to the crystal through a lead collimator with a pinhole in the middle, which has a small radius. Carbon is to be chosen as the scatterer for the Cobalt-60 machine. The carbon scatterer is suspended at the isocenter of the machine; the collimators and the detector are optically aligned with the center of the scatterer so the detector forms a 90° angle with the axis of the radiation beam from the Cobalt-60 unit.

A calibration curve, relating base line voltage on the MCA to photon energy, is to be obtained using suitable radioactive sources with the apparatus aligned and the gain of the amplifier suitably adjusted. After setting up the experiment as described in Figure 5-

13, the Cobalt-60 machine is to be switched on, and a sufficient counting time is to be taken to ensure reasonable statistical accuracy. The scatterer is then removed from the beam, and a background run is taken using the same time intervals as before. The stability of the counting system is to be checked, and with a drift of less than 1 keV, the difference between the two runs gives the scattered spectrum.

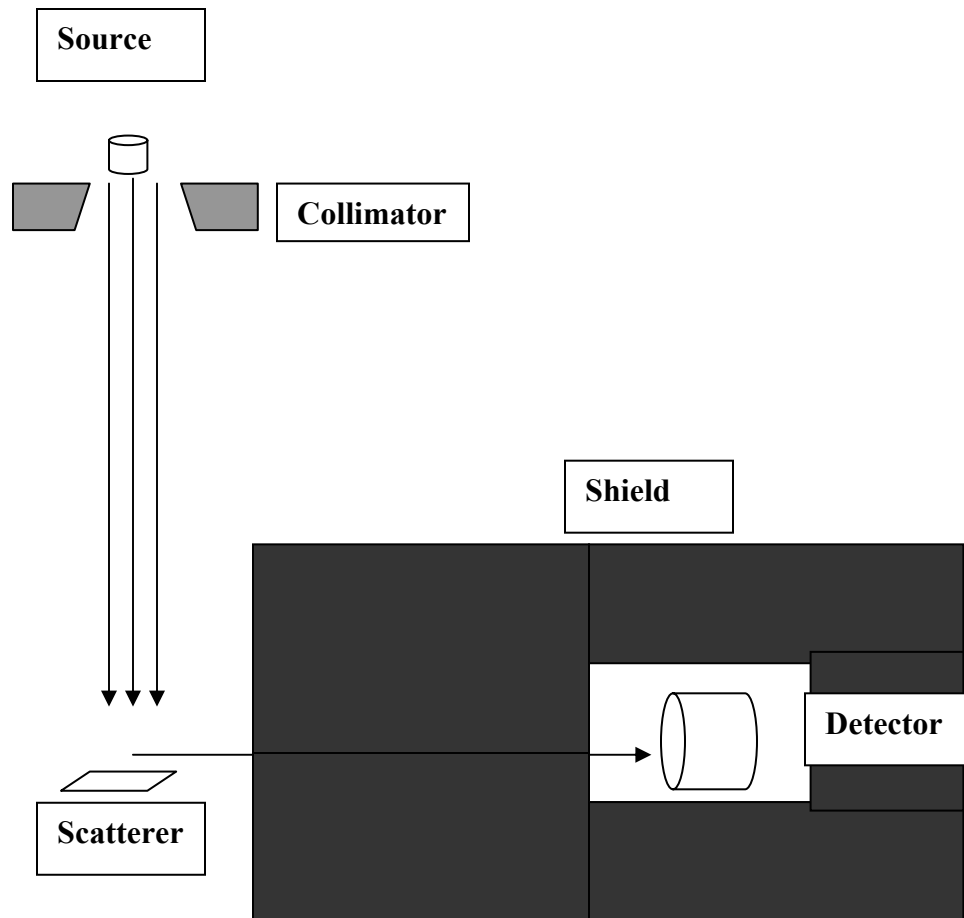


Figure 5-13. The experimental setup of coherent and incoherent scattering method (not to scale).

CHAPTER 6 CONCLUSIONS

The advantages of cobalt units, with their very low maintenance costs, lower staffing needs and minimal down time, are well known to the radiotherapy community. The net gain in reviving a safer generation of such machines could be considerable in a world having an increasing shortage of skilled radiation oncology professionals and stretched health care resources. In this research, a two-parts filter is designed to help minimize the effect of scattered photons and contamination electrons from the Cobalt-60 machine. Other techniques that reduce electron contamination were also reviewed.

A complete set of analytical formulations for the incoherent scattering spectroscopy method has been developed. The choice of scattering angle was evaluated considering the incident photon energy and the detecting efficiency of the detector. The choice of shielding and scattering material was assessed based on the radiation interaction properties of the material. It has been determined that for incoherent scattering purposes, low Z material like carbon and beryllium are more suitable than high Z material like lead and tungsten. For low Z material, in most energy ranges, the incoherent scattering process could be treated as Compton scattering, where the energy-angular correction provides a direct transformation from energy space to angular space.

After that, an experiment was designed based on the observations concluded from the analysis of the incoherent scattering spectroscopy method. This design is to be used in

future studies to benchmark and validate the results obtained from the Monte Carlo simulation.

A detailed MCNP-4C model was developed to obtain the unfiltered and filtered spectra from the Cobalt-60 machine. Skin sparing was improved for the Cobalt-60 machine by using a filter which consisted of two parts to deal with the contamination electrons and scattered photons. Using 1-mm lead filter solves the problem of electron contamination. This will reduce the surface electron contamination by 95%. The filter performs best when it is placed immediately downstream from the Cobalt-60 machine head. The existence of the electron filter will harden the photon beam by a small fraction. For a precise determination of clinical beam quality index, this photon filtering effect should be taken into account.

The primary reason that filters reduce electron contamination is that they scatter the electrons, thereby removing most contamination electrons from the beam, and similarly spreading any electrons generated over a wide area. The filter also fully stops low-energy contaminant electrons. Thus, the lead filters should be thick enough to make negligible the effect of contaminant electrons generated upstream. In this case, only those electrons generated by photon interactions in the air past the filter, and in the filter itself, contribute to the electron contamination. At the same time, the filters can be sufficiently thin that: (i) the photon beam quality is little affected, (ii) the photon dose is reduced by just a few percentages and (iii) the electron contamination generated in the filters themselves is minimized.

Using an anti-scattering grid reduced the problem of scattered photons. Using high attenuating material, such as depleted uranium, allowed maximization of the output of the

machine, and at the same time reduced the scattered photons generated in the machine head. Septa length is also a major factor in reducing the scattered photons fluence. Using longer septa increased the probability of scattered photons to be attenuated by more than one septal.

The variation of photons fluence with field size is due almost entirely to increased collimator scatter. Using the anti-scattering grid minimized this affect, and allowed the output to be almost constant for different field sizes. Different therapeutic applications require different septa thickness and length. The use of such a grid will cause a slightly non-uniform distribution photon spectrum. The best uniformity can be achieved by using a high number of septa with small holes.

APPENDIX
MCNP INPUT FILE FOR COBALT-60 MACHINE SIMULATION

Co-60 machine scattered flux spectrum simulation

C cell cards

```

1  4 -7.8      (-1 130 2 -132):(-1 132 -3) imp:p 1 $co source
2  0 (-4 133 -7 ):(-131 -7 3) imp:p 1 $ 1st void
3  3 -11.3     (-6 4 129 -2 ):(-6 4 2 -7 ):
      (-6 9 7 -7 )                               imp:p 1
4  3 -11.3     (-6 9 7 -8 ):(-9 10 7 -8 ):
      (10 7 -7 -6):(1 -7 -4 7) imp:p 1
5  3 -11.3     (-11 12 7 -8 ) imp:p 1
6  3 -11.3     (-13 14 7 -8 ) imp:p 1
7  3 -11.3     (-15 16 7 -8 ) imp:p 1
8  3 -11.3     (-17 18 7 -8 ) imp:p 1
9  3 -11.3     (-19 20 7 -8 ) imp:p 1
10 3 -11.3     (-21 22 7 -8 ) imp:p 1
11 3 -11.3     (-23 24 7 -8 ) imp:p 1
12 3 -11.3     (-25 26 7 -8 ) imp:p 1
13 3 -11.3     (-27 28 7 -8 ) imp:p 1
14 3 -11.3     (-29 30 7 -8 ) imp:p 1
15 2 -19.3     (-31 32 7 -8 ) imp:p 1
16 2 -19.3     (-33 34 7 -8 ) imp:p 1
17 2 -19.3     (-35 36 7 -8 ) imp:p 1
18 2 -19.3     (-37 38 7 -8 ) imp:p 1
19 2 -19.3     (-39 40 7 -8 ) imp:p 1
20 2 -19.3     (-41 42 7 -8 ) imp:p 1
21 2 -19.3     (-43 44 7 -8 ) imp:p 1
22 2 -19.3     (-45 46 7 -8 ) imp:p 1
23 2 -19.3     (-47 48 7 -8 ) imp:p 1
24 2 -19.3     (-49 50 7 -8 ) imp:p 1
25 2 -19.3     (-51 52 7 -8 ) imp:p 1
26 2 -19.3     (-53 54 7 -8 ) imp:p 1
27 2 -19.3     (-55 56 7 -8 ) imp:p 1
28 2 -19.3     (-57 58 7 -8 ) imp:p 1
29 2 -19.3     (-59 60 7 -8 ) imp:p 1
30 2 -19.3     (-61 62 7 -8 ) imp:p 1
31 2 -19.3     (-63 64 7 -8 ) imp:p 1
32 2 -19.3     (-65 66 7 -8 ) imp:p 1
33 2 -19.3     (-67 68 7 -8 ) imp:p 1
34 2 -19.3     (-69 70 7 -8 ) imp:p 1
35 2 -19.3     (-71 72 7 -8 ) imp:p 1

```

36 2 -19.3 (-73 74 7 -8) imp:p 1
 37 2 -19.3 (-75 76 7 -8) imp:p 1
 38 2 -19.3 (-77 78 7 -8) imp:p 1
 39 2 -19.3 (-79 80 7 -8) imp:p 1
 40 2 -19.3 (-81 82 7 -8) imp:p 1
 41 2 -19.3 (-83 84 7 -8) imp:p 1
 42 2 -19.3 (-85 86 7 -8) imp:p 1
 43 2 -19.3 (-87 88 7 -8) imp:p 1
 44 2 -19.3 (-89 90 7 -8) imp:p 1
 45 2 -19.3 (-91 92 7 -8) imp:p 1
 46 2 -19.3 (-93 94 7 -8) imp:p 1
 47 2 -19.3 (-95 96 7 -8) imp:p 1
 48 0 (-97 98 7 -8) imp:p 1
 49 2 -19.3 (-99 100 7 -8) imp:p 1
 50 0 (-101 102 7 -8) imp:p 1
 51 2 -19.3 (-103 104 7 -8) imp:p 1
 52 0 (-105 106 7 -8) imp:p 1
 53 2 -19.3 (-107 108 7 -8) imp:p 1
 54 3 -11.3 (-10 11 7 -8) imp:p 1
 55 3 -11.3 (-12 13 7 -8) imp:p 1
 56 3 -11.3 (-14 15 7 -8) imp:p 1
 57 3 -11.3 (-16 17 7 -8) imp:p 1
 58 3 -11.3 (-18 19 7 -8) imp:p 1
 59 3 -11.3 (-20 21 7 -8) imp:p 1
 60 3 -11.3 (-22 23 7 -8) imp:p 1
 61 3 -11.3 (-24 25 7 -8) imp:p 1
 62 3 -11.3 (-26 27 7 -8) imp:p 1
 63 3 -11.3 (-28 29 7 -8) imp:p 1
 64 3 -11.3 (-30 31 7 -8) imp:p 1
 65 3 -11.3 (-32 33 7 -8) imp:p 1
 66 3 -11.3 (-34 35 7 -8) imp:p 1
 67 2 -19.3 (-36 37 7 -8) imp:p 1
 68 2 -19.3 (-38 39 7 -8) imp:p 1
 69 2 -19.3 (-40 41 7 -8) imp:p 1
 70 2 -19.3 (-42 43 7 -8) imp:p 1
 71 2 -19.3 (-44 45 7 -8) imp:p 1
 72 2 -19.3 (-46 47 7 -8) imp:p 1
 73 0 (-48 49 7 -8) imp:p 1
 74 0 (-50 51 7 -8) imp:p 1
 75 0 (-52 53 7 -8) imp:p 1
 76 0 (-54 55 7 -8) imp:p 1
 77 0 (-56 57 7 -8) imp:p 1
 78 0 (-58 59 7 -8) imp:p 1
 79 0 (-60 61 7 -8) imp:p 1
 80 0 (-62 63 7 -8) imp:p 1
 81 0 (-64 65 7 -8) imp:p 1

82 0 (-66 67 7 -8) imp:p 1
 83 0 (-68 69 7 -8) imp:p 1
 84 0 (-70 71 7 -8) imp:p 1
 85 0 (-72 73 7 -8) imp:p 1
 86 0 (-74 75 7 -8) imp:p 1
 87 0 (-76 77 7 -8) imp:p 1
 88 0 (-78 79 7 -8) imp:p 1
 89 0 (-80 81 7 -8) imp:p 1
 90 0 (-82 83 7 -8) imp:p 1
 91 0 (-84 85 7 -8) imp:p 1
 92 0 (-86 87 7 -8) imp:p 1
 93 0 (-88 89 7 -8) imp:p 1
 94 0 (-90 91 7 -8) imp:p 1
 95 0 (-92 93 7 -8) imp:p 1
 96 0 (-94 95 7 -8) imp:p 1
 97 0 (-96 97 7 -8) imp:p 1
 98 0 (-98 99 7 -8) imp:p 1
 99 0 (-100 101 7 -8) imp:p 1
 100 0 (-102 103 7 -8) imp:p 1
 101 0 (-104 105 7 -8) imp:p 1
 102 0 (-106 107 7 -8) imp:p 1
 103 0 (-108 7 -8) imp:p 1
 127 3 -11.3 (-4 5 -129):(-6 4 5 -129) imp:p 1
 128 1 -5 (-130 2 -132) imp:p 1
 129 2 -19.3 (-133 3 -4 131) imp:p 1
 130 0 (-4 1 -3 129):(-1 -2 129) imp:p 1
 109 5 -5.3 -109 imp:p 1
 105 0 (6 -110 : -5 : 8) (109 -110) imp:p 1
 199 0 110 imp:p 0

1 cy 1.5 \$Co source
 2 py 4.7 \$back source plane
 3 py 7.67
 7 py 15 \$front source plane
 4 cy 20 \$void cy
 5 py 0 \$back void
 6 cy 25 \$lead cy
 8 py 20 \$front tungton
 9 ky 6 0.125 1 \$lead cone
 10 ky 6 0.12425625 1
 11 ky 6 0.121783551 1
 12 ky 6 0.119335703 1
 13 ky 6 0.116912706 1
 14 ky 6 0.11451456 1
 15 ky 6 0.112141266 1
 16 ky 6 0.109792823 1

17	ky	6	0.107469231	1
18	ky	6	0.10517049	1
19	ky	6	0.102896601	1
20	ky	6	0.100647563	1
21	ky	6	0.098423376	1
22	ky	6	0.09622404	1
23	ky	6	0.094049556	1
24	ky	6	0.091899923	1
25	ky	6	0.089775141	1
26	ky	6	0.08767521	1
27	ky	6	0.085600131	1
28	ky	6	0.083549903	1
29	ky	6	0.081524526	1
30	ky	6	0.079524	1
31	ky	6	0.077548326	1
32	ky	6	0.075597503	1
33	ky	6	0.073671531	1
34	ky	6	0.07177041	1
35	ky	6	0.069894141	1
36	ky	6	0.068042723	1
37	ky	6	0.066216156	1
38	ky	6	0.06441444	1
39	ky	6	0.062637576	1
40	ky	6	0.060885563	1
41	ky	6	0.059158401	1
42	ky	6	0.05745609	1
43	ky	6	0.055778631	1
44	ky	6	0.054126023	1
45	ky	6	0.052498266	1
46	ky	6	0.05089536	1
47	ky	6	0.049317306	1
48	ky	6	0.047764103	1
49	ky	6	0.046235751	1
50	ky	6	0.04473225	1
51	ky	6	0.043253601	1
52	ky	6	0.041799803	1
53	ky	6	0.040370856	1
54	ky	6	0.03896676	1
55	ky	6	0.037587516	1
56	ky	6	0.036233123	1
57	ky	6	0.034903581	1
58	ky	6	0.03359889	1
59	ky	6	0.032319051	1
60	ky	6	0.031064063	1
61	ky	6	0.029833926	1
62	ky	6	0.02862864	1

63	ky	6	0.027448206	1
64	ky	6	0.026292623	1
65	ky	6	0.025161891	1
66	ky	6	0.02405601	1
67	ky	6	0.022974981	1
68	ky	6	0.021918803	1
69	ky	6	0.020887476	1
70	ky	6	0.019881	1
71	ky	6	0.018899376	1
72	ky	6	0.017942603	1
73	ky	6	0.017010681	1
74	ky	6	0.01610361	1
75	ky	6	0.015221391	1
76	ky	6	0.014364023	1
77	ky	6	0.013531506	1
78	ky	6	0.01272384	1
79	ky	6	0.011941026	1
80	ky	6	0.011183063	1
81	ky	6	0.010449951	1
82	ky	6	0.00974169	1
83	ky	6	0.009058281	1
84	ky	6	0.008399722	1
85	ky	6	0.007766016	1
86	ky	6	0.00715716	1
87	ky	6	0.006573156	1
88	ky	6	0.006014002	1
89	ky	6	0.005479701	1
90	ky	6	0.00497025	1
91	ky	6	0.004485651	1
92	ky	6	0.004025902	1
93	ky	6	0.003591006	1
94	ky	6	0.00318096	1
95	ky	6	0.002795766	1
96	ky	6	0.002435422	1
97	ky	6	0.002099931	1
98	ky	6	0.00178929	1
99	ky	6	0.001503501	1
100	ky	6	0.001242563	1
101	ky	6	0.001006476	1
102	ky	6	0.00079524	1
103	ky	6	0.000608856	1
104	ky	6	0.000447322	1
105	ky	6	0.000310641	1
106	ky	6	0.00019881	1
107	ky	6	0.000111831	1
108	ky	6	4.97025E-05	1

```

129 py 4
130 cy 1 $Co source
131 ky 0 0.055 1
132 py 7.30 $front source plane
133 py 10
109 rcc 0 86 0 0 20 0 1.4 $detector
110 so 200 $air

```

```
mode p
```

```
m1 27060 1.0
```

```
m2 74184 1.0
```

```
m3 82206 1.0
```

```
m4 26000 1.0
```

```
m5 32074 1.0
```

```
sdef CEL=128 POS=0 6 0 ERG=d1 PAR=2
```

```
SI1 L 1.17 1.33
```

```
SP1 D 0.5 0.5
```

```

E0 1.00E-2 2.00E-2 3.00E-2 4.00E-2 5.00E-2 6.00E-2 7.00E-2 8.00E-2
9.00E-2 1.00E-1 1.10E-1 1.20E-1 1.30E-1 1.40E-1 1.50E-1 1.60E-1
1.70E-1 1.80E-1 1.90E-1 2.00E-1 2.10E-1 2.20E-1 2.30E-1 2.40E-1
2.50E-1 2.60E-1 2.70E-1 2.80E-1 2.90E-1 3.00E-1 3.10E-1 3.20E-1
3.30E-1 3.40E-1 3.50E-1 3.60E-1 3.70E-1 3.80E-1 3.90E-1 4.00E-1
4.10E-1 4.20E-1 4.30E-1 4.40E-1 4.50E-1 4.60E-1 4.70E-1 4.80E-1
4.90E-1 5.00E-1 5.10E-1 5.20E-1 5.30E-1 5.40E-1 5.50E-1 5.60E-1
5.70E-1 5.80E-1 5.90E-1 6.00E-1 6.10E-1 6.20E-1 6.30E-1 6.40E-1
6.50E-1 6.60E-1 6.70E-1 6.80E-1 6.90E-1 7.00E-1 7.10E-1 7.20E-1
7.30E-1 7.40E-1 7.50E-1 7.60E-1 7.70E-1 7.80E-1 7.90E-1 8.00E-1
8.10E-1 8.20E-1 8.30E-1 8.40E-1 8.50E-1 8.60E-1 8.70E-1 8.80E-1
8.90E-1 9.00E-1 9.10E-1 9.20E-1 9.30E-1 9.40E-1 9.50E-1 9.60E-1
9.70E-1 9.80E-1 9.90E-1 1.00 1.01 1.02 1.03 1.04 1.05 1.06 1.07
1.08 1.09 1.10 1.11 1.12 1.13 1.14 1.15 1.16 1.17 1.18 1.19 1.20
1.21 1.22 1.23 1.24 1.25 1.26 1.27 1.28 1.29 1.30 1.31 1.32 1.33
1.34 1.35 1.36 1.37 1.38 1.39 1.40

```

```
f4:p 109
```

```
nps 30000000
```

```
totnu
```

```
print
```

LIST OF REFERENCES

- Andreo P 1991 Monte Carlo techniques in medical radiation physics Phys Med Biol **36** 861-920
- Attix F H, Lopz F, Owolabi S, and Paliwal B R 1983 Electron contamination in Co-60 gamma ray beams Med Phys **10** 301-306
- Bentley R E, Jones J C and Lillicrap S C 1967 X-ray spectra from accelerators in the range 2 to 6 MeV Phys Med Biol **12** 301-314
- Biggs P J 1987 The forward production of high-energy electrons from megavoltage photon beams Med Phys **14** 767-771
- Biggs P J and Ling C C 1979 Electrons as the cause of the observed d_{\max} shift with field size in high energy photon beams Med Phys **6** 291-295
- Briesmeister J F (ed) 1997 MCNP-A General Monte Carlo N-particle Transport Code Version 4B LA-12625-M. Los Alamos, NM: Los Alamos National Laboratory
- Chantler C T 1995 Theoretical form factor, attenuation, and scattering tabulation for $Z = 1-92$ from $E = 1-10$ eV to $E = 0.4 - 10$ MeV J Phys Chem Ref Data **24** (1995) 71-581
- Ciesielski B, Reinstein L E, Wielopolski L, and Meek A 1989 Dose enhancement in buildup region by lead, aluminum, and lucite absorbers for 15 MV photon beam Med Phys **16** 609-613
- DeMarco J J, Solberg T D and Smathers J B 1998 A CT-based Monte Carlo simulation tool for dosimetry planning and analysis Med Phys **25** 1-11
- Faddegon B A, Ross C K and Rogers D W O 1991 Angular distribution of bremsstrahlung from 15 MeV electrons incident on thick target of Be, Al and Pb Med Phys **18** 727-739
- Galbraith D M and Rawlinson J A 1985 Direct measurement of electron contamination in cobalt beams using a charge detector Med Phys **12** 273-280
- Han K, Ballon D, Chui C and Mohan R 1987 Monte Carlo simulation of a Cobalt-60 beam Med Phys **14** 414-419

- Harper N R, Metcalfer P E, Hoban P W, and Round W H 1991 Electron contamination in 4 MV and 10 MV radiotherapy X-ray beams Australas Phys Eng Sci Medicine **14** 141-145
- Hubbell, J.H., Veigle, W.J., Briggs, E.A., Brown, R.T., Cromer, D.T., Howerton, R J 1975 Atomic form factor, incoherent scattering functions, and photon scattering cross section J Phys Chem Ref Data **4** 471-538.
- Klevenhagen S C, D'Souza D, and Bonnefoux I 1991 Complications in low energy x-ray dosimetry caused by electron contamination Phys Med Biol **36** 1111-1116
- Kosunen A and Rogers D W O 1993 Beam Quality Specification for Photon Beam Dosimetry Med Phys **20** 1181-1188
- Landry D J and Anderson D W 1991 Measurement of accelerator bremsstrahlung spectra with a high-efficiency Ge detector Med Phys **18** 527-532
- Leung P M K and Johns H E 1977 Use of electron filters to improve buildup characteristics of large fields from Cobalt-60 beam Med Phys **4** 441-444
- Levy L B, Waggener R G, McDavid W D and Payne W H 1974 Experimental and calculated bremsstrahlung spectra from a 25 MeV linear accelerator and a 19 MeV betatron Med Phys **1** 62-67
- Levy L B, Waggener R G, and Wright A E 1976 Measurement of primary bremsstrahlung spectrum from an 8 MeV linear accelerator Med Phys **3** 173-175
- Lewis R D, Ryde S J S, Hancock D A and Evans C J 1999 An MCNP-based model of a linear accelerator x-ray beam Phys Med Biol **44** 1219-1230
- Ling C C and Biggs P J 1979 Improving the buildup and depth-dose characteristics of high energy photon beams by using electron filters Med Phys **6** 296-301
- Ling C C, Schell M C, and Rustgi S N 1982 Magnetic analysis of the radiation components of a 10 MV photon beam Med Phys **9** 20-26
- Liu H H, Mackie T R and McCullough E C 1997 A dual source photon beam model used convolution/superposition dose calculations for clinical megavoltage x-ray beam Med Phys **24** 1960-74
- Lovelock D M, Chui C S and Mohan R 1995 A Monte Carlo model of photon beams used in radiation therapy Med Phys **22** 1387-94
- Mackie T R 1990 Applications of Monte Carlo method in radiotherapy The Dosimetry of Ionizing Radiation, ed K R Kase, B Bjangard and F H Attix New York: Academic **3** pp 541-620

- Mohan R, Chui C, and Lidofsky L 1986 Differential pencil beam dose computation model for photons Med Phys **13** 64-73
- Mora G M, Maio A and Rogers D W O 1999 Monte Carlo simulation of a typical Cobalt-60 therapy source Med Phys **26** 2494-2502
- Morin R L (ed) 1988 Monte Carlo Simulation in the Radiological Sciences CRC press Boca Raton
- Nilsson B, 1985 Electron contamination from different material in high energy photon beams Phys Med Biol **30** 139-151
- Parthasaradhi K, Prasad S G, Rao B M, Lee Y, Ruparel R, and Garces R 1989 Investigation on the reduction of electron contamination with a 6 MV x-ray beam Med Phys **16** 123-125
- Petti P L, Goodman M S, Gabriel T A, Mohan R 1983a Investigation of buildup dose from electron contamination for the clinical photon beams Med Phys **10** 18-24
- Petti P L, Goodman M S, Sisterson J M, Biggs P J, Gabriel T A, Mohan R 1983b Source of electron contamination for the Clinac-35 25 MV photon beams Med Phys **10** 856-861
- Rao B M, Prasad S G, Parthasaradhi K, Lee Y, and Ruparel R 1988 Investigation on the near surface dose for three 10 MV x-ray beam accelerator with emphasis on the reduction of electron contamination Med Phys **15** 246-249
- Rogers D W O, Faddagon B A, Ding G X, Ma C M, Wei J and Mackie T R 1994 BEAM: A Monte Carlo code to simulate radiotherapy treatment units Med Phys **22** 503-524
- Williamson J F, Deibel F C, and Morin R L 1984 The significance of electron binding corrections in Monte Carlo photon transport calculations Phys Med Biol **29** 1063-1073
- Yorke E D, Ling C C, and Rustgi S 1985 air-generated electron contamination of 4 and 10 MV photon beam: a comparison of theory and experiment Phys Med Biol **30** 1305-1314

BIOGRAPHICAL SKETCH

Ahmad Al-Basheer was born in 1978 in Ramtha City, Jordan, in the heart of the Middle East. Generations of his family have made Ramtha their hometown for centuries. This city, which borders Syria and Jordan, is the gateway to the desert region of the Middle East.

Ahmad is the oldest of eight children, and his parents, Khaled and Fatima, are both involved in educational careers; both are school principals. Ahmad was involved not only in traditional educational venues, but also in chess, soccer, reading and poetry. Ahmad competed in several reading and poetry contests throughout his schooling; he won the National Award for high school students for Best Poet.

Ahmad graduated from Jordan University for Science and Technology with a Bachelor of Science degree in applied physics in 2000. Upon graduation, he spent one year as a physics teacher at the Yarmouk University Model School. In January, 2002, Ahmad was granted admission to the graduate program in the Department of Nuclear and Radiological Engineering at the University of Florida.